Microstructure of BAlN and InGaN Epilayers for Optoelectronic Applications

by

Shuo Wang

A Dissertation Presented in Partial Fulfillment
of the Requirements for the Degree
Doctor of Philosophy

Approved July 2018 by the
Graduate Supervisory Committee:

Fernando A. Ponce, Chair
Jose Menendez
Martha McCartney
Peter Rez

ARIZONA STATE UNIVERSITY

August 2018

ABSTRACT

In this dissertation, various characterization techniques have been used to investigate many aspects of the properties of III-nitride materials and devices for optoelectronic applications.

The first part of this work is focused on the evolution of microstructures of BAlN thin films. The films were grown by flow-modulated epitaxy at 1010 ^{o}C, with B/(B+Al) gas-flow ratios ranging from 0.06 to 0.18. The boron content obtained from X-ray diffraction (XRD) patterns ranges from x = 0.02 to 0.09, while Rutherford backscattering spectrometry (RBS) measures x = 0.06 to 0.16. Transmission electron microscopy indicates the sole presence of the wurtzite crystal structure in the BAlN films, and a tendency towards twin formation and finer microstructure for B/(B+Al) gas-flow ratios greater than 0.15. The RBS data suggest that the incorporation of B is highly efficient, while the XRD data indicate that the epitaxial growth may be limited by a solubility limit in the crystal phase at about 9%. Electron energy loss spectroscopy has been used to profile spatial variations in the composition of the films. It has also located point defects in the films with nanometer resolution. The defects are identified as B and Al interstitials and N vacancies by comparison of the observed energy thresholds with results of density functional theory calculations.

The second part of this work investigates dislocation clusters observed in thick $In_xGa_{1-x}N$ films with $0.07 \leq x \leq 0.12$. The clusters resemble baskets with a higher indium content at their interior. Threading dislocations at the basket boundaries are of the misfit edge type, and their separation is consistent with misfit strain relaxation due the difference

in indium content between the baskets and the surrounding matrix. The base of the baskets exhibits no observable misfit dislocations connected to the threading dislocations, and often no net displacements like those due to stacking faults. It is argued that the origin of these threading dislocation arrays is associated with misfit dislocations at the basal plane that dissociate, forming stacking faults. When the stacking faults form simultaneously satisfying the crystal symmetry, the sum of their translation vectors does add up to zero, consistent with our experimental observations.

ACKNOWLEDGEMENTS

I would like to thank Dr. Fernando A. Ponce for offering me this great opportunity to study and research as a Ph.D. student at Arizona State University. I did not only gain knowledge and skills in physical science, but also deepened my understanding in methods of research and management of life. I would also like to thank the members of my graduate supervisory committee, Dr. Peter Rez, Dr. Martha McCartney, and Dr. José Menendez, for offering me great help towards the completion of my doctoral degree.

I would like to thank the former group members: Dr. Alec Fischer, Dr. Ti Li, Dr. Jingyi Huang, Dr. Reid Juday, Dr. Yong Wei, Dr. Hongen Xie; and the current members: Hanxiao Liu, Po-Yi Su, and Shanthan Alugubelli. You are not only good colleagues, from whom I learned and with whom I cooperated, but you are also good friends, with whom I spent six wonderful years.

I would like to thank Dr. David Smith of the Department of Physics at ASU; Dr. Katia March, of the Eyring Materials Center at ASU; Dr. Heather McFavilen, of PhotoNitride Devices Inc.; and Dr. W. Alan Doolittle and the members of his research group at the Georgia Institute of Technology; Dr. Russell D. Dupuis, and the members of his research group at the Georgia Institute of Technology: Dr. Xiaohang Li, Dr. Theeradetch Detchprohm, and Yuh-Shiuan Liu. Thank you for the invaluable opportunities of collaboration, and more importantly, the experience of exchanging knowledge and ideas.

I would like to thank my parents, and all my friends, for their support in my work and life.

TABLE OF CONTENTS

Page

CHAPTER Page

CHAPTER Page

LIST OF TABLES

LIST OF FIGURES

Figure Page

Figure Page

Figure Page

Chapter 1 Introduction

The III-nitride semiconductors have been widely used in optoelectronic devices. One advantage of this material system is that the III-nitride semiconductors usually have direct band gaps, making the radiative recombination and light absorption in the material far more effective than indirect band gap materials, such as silicon. Also their band gaps cover the range from infrared to ultraviolet, as shown in Figure 1.1.

A large amount of research has been carried out on the properties of the III-nitride semiconductors, and many applications have been realized with the materials. Light emitting diodes (LEDs) emitting in different visible light regions and ultraviolet are produced with Al-Ga-In-N alloys.[1,2] Laser diodes (LDs) in blue and ultraviolet range have also been achieved using InGaN quantum wells.[3,4] InGaN alloys have been demonstrated as a full-solar-spectrum material system for multijunction solar cells.[5]

Most of the research on III-nitride semiconductors has focused on the Al-Ga-In-N alloys. The GaN-based alloys, AlGaN and InGaN, with low aluminum and indium content, have been successful in providing high quality materials for device applications. For instance, blue light emitting devices and blue laser diodes are currently commercially available, making possible the white LEDs for illumination that replaces incandescent lamps with significant savings in electric power, and the blue-laser diode technology for high-density optical storage.

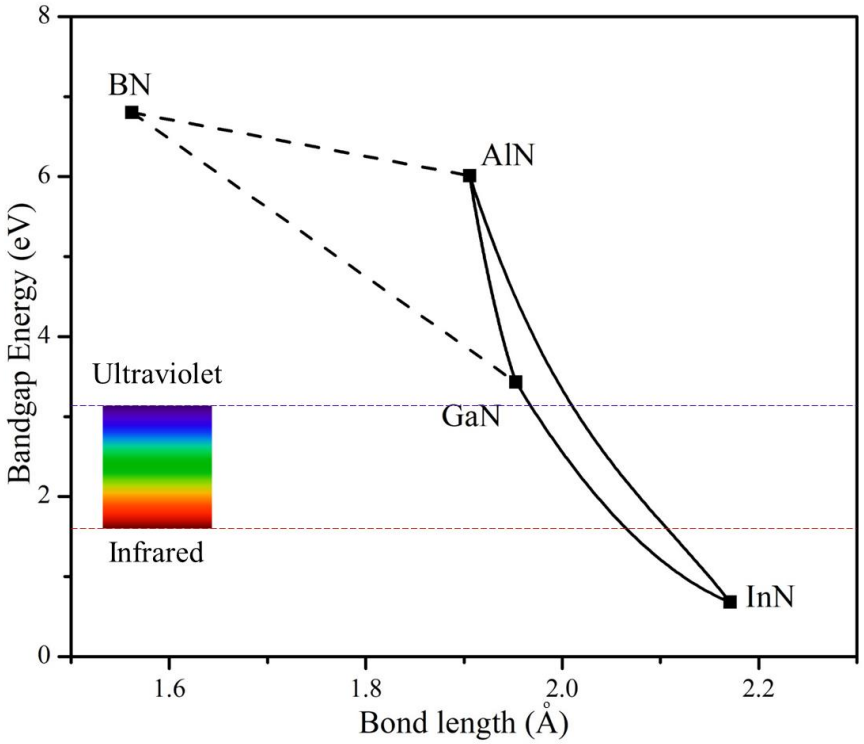

Figure 1.1. Chemical bond lengths and band gap energies of III-nitride semiconductors, adapted from Ref. 6. The data of BN is from Ref. 7.

With respect to the wider band gaps in Figure 1.1, there is much interest in expanding the knowledge base of these materials into boron-containing III-nitride alloys, in order to provide additional functionality. For example, B incorporation in AlN layers can be potentially used in ultraviolet (UV) vertical-cavity surface-emitting lasers (VCSELs). High reflectivity distributed Bragg reflectors (DBRs) are essential components for the VCSELs, as shown in Figure 1.2. BAlN alloys are promising materials for the DBRs because: (1) the large bandgap shown in Figure 1.1 provides transparency of the BAlN layers in the UV region, and (2) incorporating B into AlN films causes considerable reduction in the refractive index.[8] The desired BAlN layers should possess at least the following properties:

(1) wurtzite structure to be epitaxially grown on AlN layers, (2) high B content to provide a large difference in the refractive indices, and (3) thickness larger than a quarter of wavelength to form a DBR layer shown in Figure 1.1. However, previous reports indicate a 2.8% low solubility limit of B in the AlN films.[9] And for a higher B content of 12%, only the first 10 nm of the BAlN films exhibit wurtzite single crystal structure.[10,11] So, a detailed study of the B-containing III-nitride alloys is necessary on the structural properties to take use of the potential advantages of the alloy system.

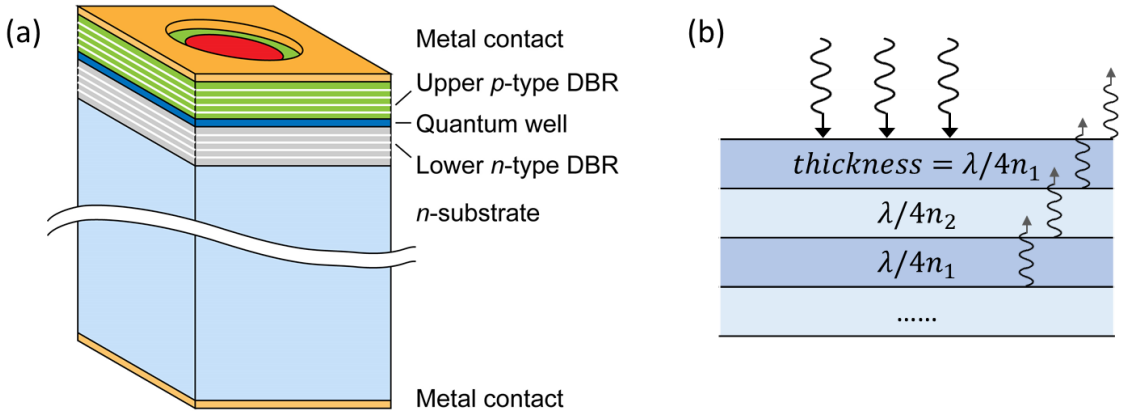

Figure 1.2. (a) Schematic drawing of a VCSEL structure. (b) Schematic drawing of a DBR structure.

Another important field of the III-nitride semiconductors is the InGaN alloy system, with high indium content, which can be potentially used in high efficiency solar cells under concentrated sun light, due to the advantages of high carrier mobility, high thermal conductivity, and high temperature resistance.[12] However, a single-junction solar cell has an efficiency limit ~30%, known as the Shockley-Queisser limit.[13] A multi-junction solar cell can potentially exceed this limit, where the InGaN layers used as the active regions need to have various bandgap energies, thus In contents, covering a large range of the

visible spectrum. For InGaN layers grown on GaN substrate, there is a specific In content range, $0.07 \leq [In] \leq 0.12$, which is the intermediate range between elastic deformation and full plastic relaxation. It is therefore of much interest the study of strain relaxation mechanisms in InGaN thick films in that range of indium composition.

This dissertation presents the results of research performed on the structural properties of two III-nitride alloy systems, the BAlN alloys and the InGaN alloys.

Chapter 2 gives a brief introduction to the characterization techniques used in these studies, covering microscopy, spectroscopy, and computational methods for structural, optical, and electronic properties.

Chapter 3 discusses the evolution of the microstructure of BAlN thin films with increasing boron content. The films maintain a wurtzite structure for films with thickness of 50 nm, with as high as 18% boron composition introduced during growth. The BAlN films tend to grow into finer grains with larger tilting angles, with higher B content. The B spatial distribution is inhomogeneous, with possible higher B contents in the tilted grains, and B segregation at the grain boundaries.

In Chapter 4, the study of BAlN thin films continues into identifying the point defects. In the very low-loss region of the electron energy loss spectra (EELS), several peaks are observed below the bandgap threshold. This could be the first time in history for the direct observation of point defects by EELS. Density functional theory calculations are used to relate these peaks to B and Al interstitials and N vacancies.

Chapter 5 deals with the InGaN thin films with indium contents in the range of $0.07 \leq [In] \leq 0.12$. A unique dislocation cluster, *dislocation basket* is observed. While the rest

of the film is strained, the inside of the baskets exhibit relaxation, as well as a higher indium content. A model has been developed to explain the formation of the baskets. In this model, a misfit dislocation on the basal plane connects two threading dislocations. The basal plane misfit dislocation can dissociate into a stacking fault and a loop of partial dislocations. When the dissociation is symmetric and simultaneous, no stacking fault displacement results in the basket base, as observed experimentally.

Chapter 6 summarizes the research work, and proposes possible future works on these material systems.

A list of publications during my Ph.D. dissertation research is provided in Appendix I.

Chapter 2 Characterization Techniques

Many different characterization techniques are needed to acquire and correlate the properties of the materials and devices. Here I describe several techniques involved in my graduate study, with some details related to my research.

2.1 Transmission electron microscopy (TEM)

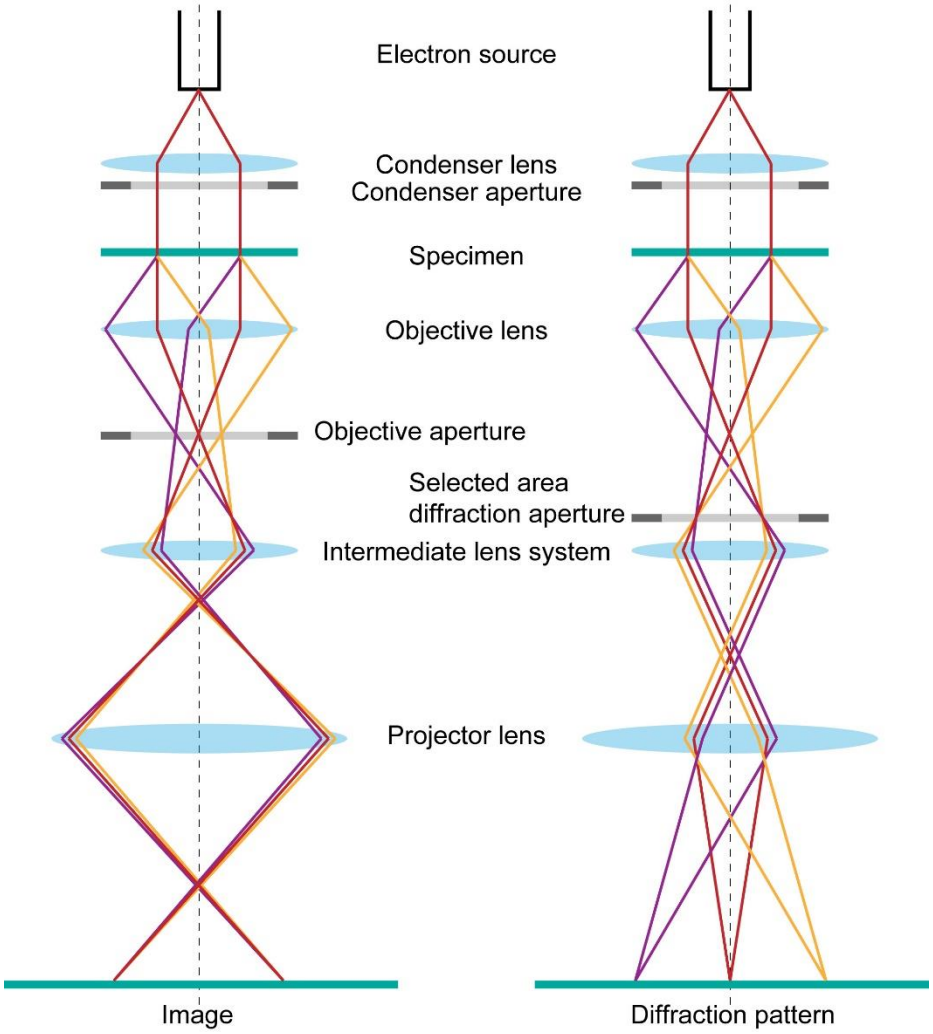

Figure 2.1. Schematic ray diagrams of TEM. Adapted from Ref. 14.

TEM is a technique in which a beam of electrons is transmitted through a specimen to form an image. Due to the short de Broglie wavelength of electrons, TEM has a

significantly higher resolution than optical microscopes, and is widely used in the study of structures and defects in semiconductor materials. Schematic drawings of the ray diagrams are shown in Figure 2.1. The condenser lens collects electrons generated by the source, and forms parallel or convergent beam on the specimen. The electrons after the objective lens form diffraction patterns at the back focal plane, and images at the image plane. Then the following lenses project the diffraction patterns or images onto the screen. Several important TEM techniques are discussed below.

2.1.1 Electron diffraction pattern

The diffraction pattern can be seen as the projection of Ewald's sphere on the screen. Each spot of the pattern corresponds to a reciprocal lattice point on or close to the sphere in the reciprocal space. In the real space, they are related to the Bragg reflection by a specific set of planes. The sample is usually thin so the scattering is elastic, while in thick samples inelastic scattering can happen, where electrons lose energy. Due to inelastic scattering, a Kikuchi pattern which consists of intersecting bands superimposes on the set of spots. The Kikuchi pattern are formed by the electrons which are scattered at exact Bragg conditions so the bands are good indication of the crystal orientation. The crystal orientation and the beam direction can be aligned by referring to the diffraction spots and the Kikuchi bands.

2.1.2 Large-angle convergent-beam electron diffraction (LACBED)

In convergent-beam electron diffraction, the incident beam converges strongly on the specimen, instead of being close to a plane wave as is in conventional electron diffraction. The diffraction spots become disks and contain more information in the reciprocal space.

In LACBED, the specimen is moved away from the eucentric plane, in which information about both the image and the diffraction pattern is visible at the same time.[15] A schematic drawing of identifying dislocations with LACBED is shown in Figure 2.2.

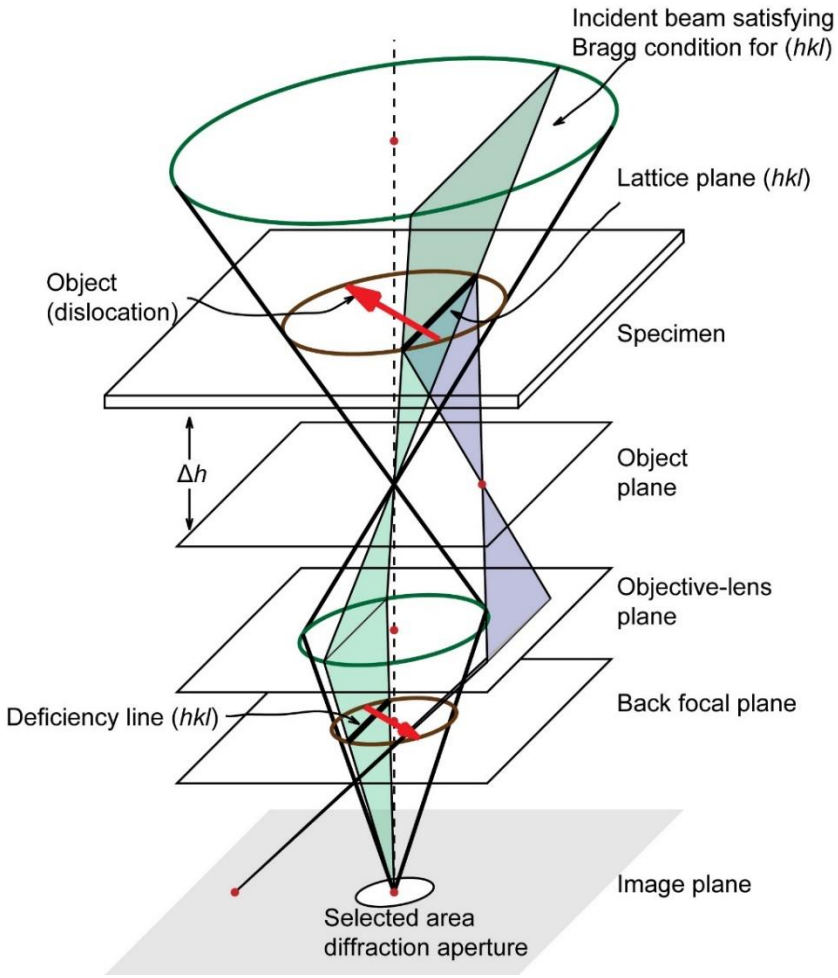

Figure 2.2. Schematic ray diagram of LACBED for identifying dislocations. Adapted from Ref. 14.

The specimen is illuminated by a large-angle and defocused incident beam. A plane of incident beam can satisfy the Bragg condition of a certain set of lattice planes (*hkl*) of the sample, and diffract away from the transmitted beam. Then the transmitted beam is selected by the selected-area diffraction aperture. So the plane of beam diffracted away is

not included to form the image, leaving a deficient line in the LACBED pattern. When a dislocation line L with a Burgers vector of $\boldsymbol{b}$ cuts the deficient line $\boldsymbol{g}$, a splitting will occur in the pattern, as seen in Figure 2.3. The number of intermediate fringes n is given by the Cherns and Preston rule: $|\boldsymbol{g} \cdot \boldsymbol{b}| = n$.[16] The sign of $|\boldsymbol{g} \cdot \boldsymbol{b}|$ can also be determined by the direction of the dislocation, the positive direction of the deviation parameter and the asymmetric splitting at intersection. By obtaining three $\boldsymbol{g} \cdot \boldsymbol{b}$ equations with different $\boldsymbol{g}$'s, the Burgers vector $\boldsymbol{b}$ can be solved.

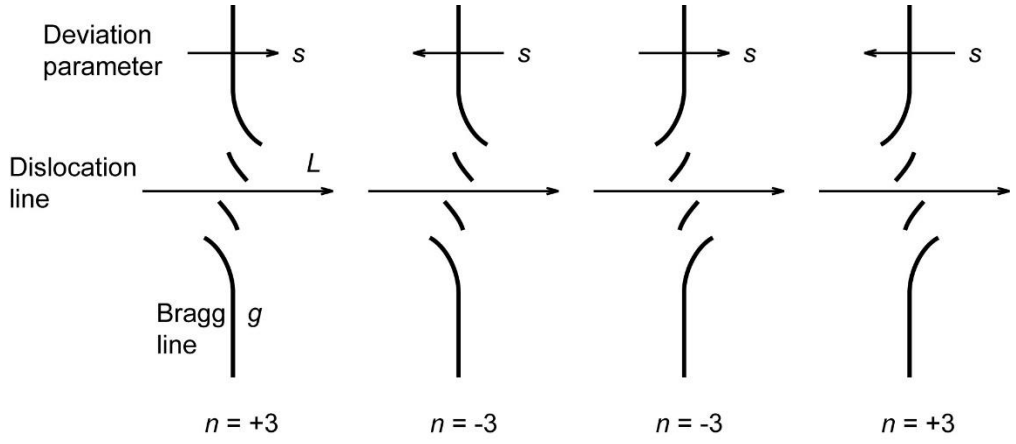

Figure 2.3. Schematic drawing of Cherns and Preston rules which allow the identification of the sign of n. Adapted from Ref. 17.

2.1.3 Diffraction contrast TEM

The sample exhibits diffraction contrast when the electron beam undergoes Bragg diffraction. One way to acquire diffraction contrast is to take two-beam images, where the sample is usually tilted to a so called "two-beam condition" to excite only one strong diffraction beam. The strong diffracted beam is selected by an aperture in the back focal plane to form a two-beam dark-field (DF) image, or the transmitted beam is selected for a two-beam bright-field (BF) image. The contrast is uniform in regions where the sample is

uniform with no defects. In the region that is close to a defect such as a dislocation, local bending of crystal planes diffracts the electron beam differently and a dark contrast in the BF image or a bright contrast in a DF image is observed. The Burgers vector of defects can be inferred by comparing the contrast of the defect under different diffraction conditions.[18] For example, the visibility of a dislocation with Burgers vector $\boldsymbol{b}$ under diffraction condition $\boldsymbol{g}$ depends on the value of $\boldsymbol{g} \cdot \boldsymbol{b}$. If $\boldsymbol{g} \cdot \boldsymbol{b} = 0$ meaning that the Burgers vector is parallel to the reflection planes, no contrast is produced.

2.1.4 Phase contrast TEM

Phase contrast TEM is also referred to as high-resolution TEM (HRTEM), since it's capable of seeing atomic columns in crystals, providing a powerful tool to study the interface, defects, etc. In high resolution TEM, a virtually parallel electron beam passes the sample during which the wave front of the plane wave is modified by the periodic atomic potential. The electron wave closer to the atomic columns travels faster and a phase advance is resulted. If the sample is thin enough, it can be regarded as a phase object which produce a wave with a spatially dependent phase shift at the exit surface:[19]

$$\Psi_{exit} = \exp(i\sigma V_z) \qquad (2.1)$$

where V_z is the position dependent projected crystal potential, the interaction constant $\sigma = \lambda me/(2\pi\hbar^2)$ is a function of electron wavelength. The image of the wave at the exit surface is imaged by the objective lens and magnified by the projection lens onto the screen.

2.1.5 Example of TEM analysis

As an example, TEM analysis was carried out on MBE GaN regrowth layers on top of GaN template, using a CM200 TEM operated at 200keV.*

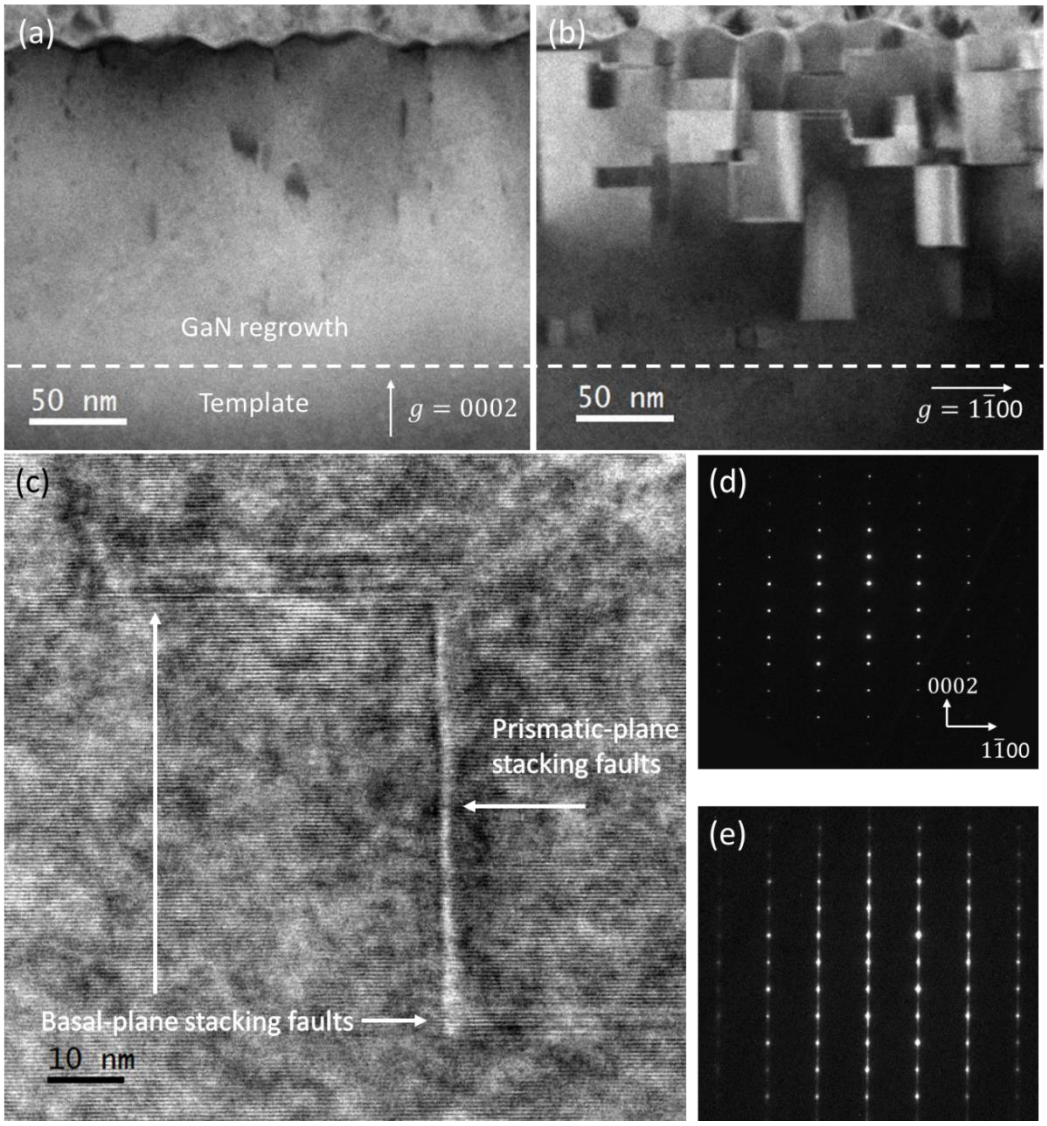

Figure 2.4. TEM analysis of a GaN regrowth layer. (a) Two-beam bright-field images at $g = 0002$ condition with only a few defects visible. (b) Two-beam bright-field images at $g = 1\bar{1}00$ condition showing basal-plane stacking faults. (c) HRTEM image showing

* The samples were grown by Dr. W. Alan Doolittle, at School of Electrical and Computer Engineering, Georgia Institute of Technology.

basal-plane and prismatic-plane stacking faults. (d) Diffraction pattern at $[11\bar{2}0]$ zone axis of wurtzite structure. (e) Diffraction pattern of a GaN film with much higher density of stacking faults.

By comparing Figure 2.4(a) and (b), the horizontal lines in (b) are identified as basal-plane stacking faults, and the vertical lines in both (a) and (b) may be prismatic stacking faults. Similar to dislocations, the visibility of stacking faults under diffraction contrast is determined by the value of $\boldsymbol{g} \cdot \boldsymbol{R}$, where $\boldsymbol{R}$ is the displacement vector of the stacking fault. Unlike dislocations, the stacking faults are invisible when $\boldsymbol{g} \cdot \boldsymbol{R}$ equals any integer.[20] The HRTEM image in Figure 2.4(c) exhibits atomic arrangement near the stacking faults. For a more obvious view of the defects, image processing such as FFT filtering can be used to show individual lattice planes. Figure 2.4(d) is a selected area diffraction pattern of the sample. The pattern shows hardly any difference from a diffraction pattern of a perfect GaN crystal, because the density of defects in this sample is not high enough. In contrast, Figure 2.4(e) is from a GaN regrowth layer in which the stacking fault density is about two orders of magnitude higher than the one in (b). Streaks can be seen along the $[0002]$ direction, indicating loss of symmetry and periodicity in this direction, caused by high density stacking faults.

2.2 Scanning transmission electron microscopy (STEM)

STEM is like conventional TEM, where images are formed by electrons passing through a sufficiently thin specimen. However, in STEM the electron beam is focused to a fine spot which is then scanned over the sample in a raster, as shown in Figure 2.5. Various signals are generated inside the STEM column and are collected by different detectors, as

illustrated in Figure 2.6. In addition to structural information, STEM also provides signals of compositional properties. Several useful tools are discussed below.

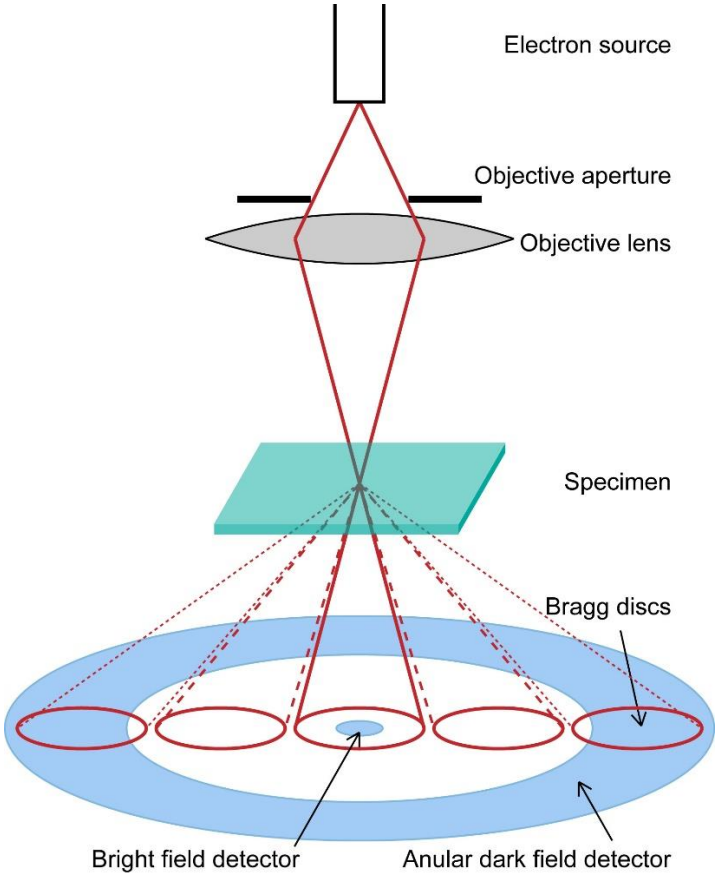

Figure 2.5. Schematic ray diagram of STEM.

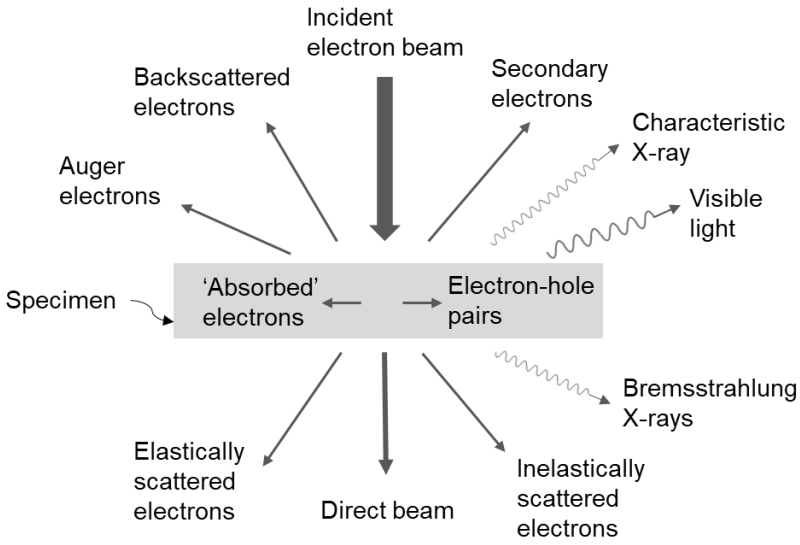

Figure 2.6. Signals generated when the electron beam interacts with the thin specimen. Adapted from Ref. 14.

2.2.1 High-angle annular dark-field (HAADF)

In HAADF, images are formed by fore-scattered electrons incident on an annular detector, which lies outside of the path of the directly transmitted beam, as shown in Figure 2.5. The scattering angle of the electrons is typically >50mrad (~3^{o}), where Braggs effects are negligible and diffraction contrast is avoided.[14] The contrast is directly related to the atomic number *Z*,[21] making HAADF images more straightforward to interpret than HRTEM images, in which simulation is needed to aid interpretation

2.2.2 Energy dispersive X-ray (EDX) spectroscopy

In EDX, an X-ray spectrometer is used to detect the characteristic X-rays emitted by elements in the sample as they are ionized by high energy electrons. EDX can also be performed in a TEM, but requires tedious switch between TEM-image and focused-spot analysis mode. So the STEM mode is better for mapping the elements using EDX.

One limitation for EDX is the challenges in analyzing light elements, including boron. The low-energy X-rays are likely to be absorbed by the specimen before they exit the surface, or by the window and other components of the detector when they manage to reach the detector.

2.2.3 Electron energy loss spectrometry (EELS)

EELS is the analysis of the energy distribution of electrons that have come through the specimen.[14] The electrons may have lost no energy, or may have experienced inelastic collisions. The low-loss region (below several tens of eV) of the spectrum contains electronic information from conduction and valence-band electrons. The rest of the spectrum, high-loss region contains elemental information and also details about bonding and atomic distribution. The energy resolution in EELS is significantly higher than EDX, and is sufficient for the fine structure of ionization edges. So EELS can be used for chemical mapping, in addition to elemental mapping. Also, EELS is able to detect and quantify all elements, making possible of the analysis of light elements, such as boron.

Some disadvantages of EELS over EDX include the requirement of very thin specimen, and the complexity in processing the spectra.

2.3 X-ray diffraction (XRD)

XRD is used for determining the structure of a crystal, in which the crystalline atoms cause the incident X-ray beams to diffract into many specific directions. For the special case of epitaxial thin films with known structures, $\theta/2\theta$ scans are widely used. As shown in Figure 2.7, the sample angle ω and the detector angle 2θ are coupled and rocked simultaneously, while keeping the X-ray source fixed. The X-ray source and the detector

are both forming an angle of θ with respect to the sample surface. Considering the Bragg's law

$$\lambda = 2d \sin\theta \qquad (2.2)$$

the acquired XRD spectrum will show a peak if the lattice plane separation d and the angle θ satisfy the Bragg's condition. Then the composition x of an alloy, for example $Al_xGa_{1-x}N$, can be related to d via Vegard's law, assuming that a linear relation exist between the crystal lattice constant of the alloy and the elemental concentration.

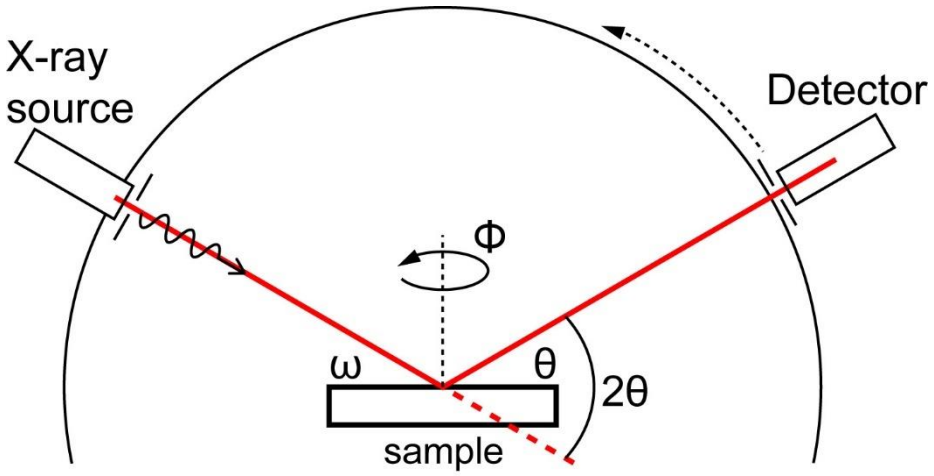

Figure 2.7. Schematic drawing of the geometry of the XRD $\theta/2\theta$ scan.

The $\theta/2\theta$ scans can also provide information about crystallite sizes, using Scherrer's equation[22]

$$\varepsilon = \lambda / b \cos\theta \qquad (2.3)$$

where ε is the apparent crystallite size, b is the broadening of peak after the correction of instrumental broadening. Note that the $\theta/2\theta$ scans with mosaic crystals will mostly reveal only reflections from crystal planes parallel to the sample surface.[23]

Reciprocal space mapping is different from a $\theta/2\theta$ scan, where the ω and 2θ are rocked independently. The intensity in the 2D space of ω and 2θ can reveal the strain relaxation in the epitaxial thin films.

2.4 Rutherford backscattering spectrometry (RBS)

RBS is used to determine the structure and composition of materials by measuring the backscattering of a beam of high energy ions impinging on a sample. The backscattering is described as an elastic, hard-sphere collision between a high kinetic energy particle from the incident beam (the projectile) and a stationary particle located in the sample (the target). The scattered particle has the kinetic energy

$$E_1 = kE_0, k = \left(\frac{m_1 \cos\theta + \sqrt{m_2^2 - m_1^2 \sin^2\theta}}{m_1 + m_2}\right)^2 \quad (2.4)$$

where particle 1 is the projectile, particle 2 is the target nucleus, and θ is the scattering angle of the projectile. The probability of scattering event is given by the differential cross-section[24]

$$\frac{d\omega}{d\Omega} = \left(\frac{Z_1 Z_2 e^2}{4E_0}\right)^2 \frac{1}{(\sin\theta/2)^4} \quad (2.5)$$

where Z_1 and Z_2 are the atomic numbers of the incident and target nuclei.

The energy loss of the backscattered ion is also affected by friction, i.e. the stopping power of the sample electrons. If the incident ion is backscattered by a specimen atom at depth X, the additional energy loss will be[24]

$$\Delta E = X[k\varepsilon(\bar{E}_{in}) + \varepsilon(\bar{E}_{out})/\cos\theta] \quad (2.6)$$

where $\varepsilon(\bar{E}_{in})$and $\varepsilon(\bar{E}_{out})$ are the stopping cross-sections of the incoming and outgoing path.

Figure 2.8 shows a schematic drawing of the geometry of the RBS chamber. Typical incident beam is composed of He^{++} ions with several MeV energies.

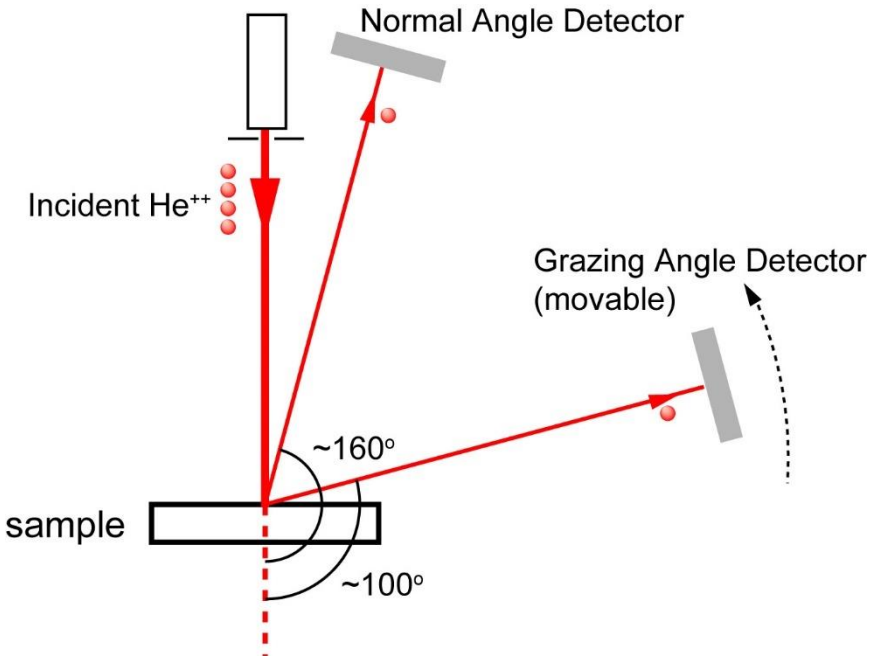

Figure 2.8. Schematic drawing of the geometry of the RBS measurement.

The detector collects spectra of numbers of backscattered ions with certain energy, i.e. *N(E)* vs. *E* as shown in Figure 2.9. First, the energy of detected He^{++} ions is determined by the nature of atoms in the specimen, so different atomic species possess different signature energies, seen as separate peaks in the spectrum. Second, the backscattering energy is affected by friction. The deeper an ion travels into the specimen, the more kinetic energy is dissipated. So, a certain peak has a width related to the thickness of the layer containing the certain atoms. In summary the RBS spectra are depth profiles of elements. In Figure 2.8, for the He^{++} ions backscattered at the same depth in the specimen, the ions traveling at a grazing angle are affected by friction more than those traveling at a larger angle. So the grazing angle detector provides spectra where the effect of depth is amplified.

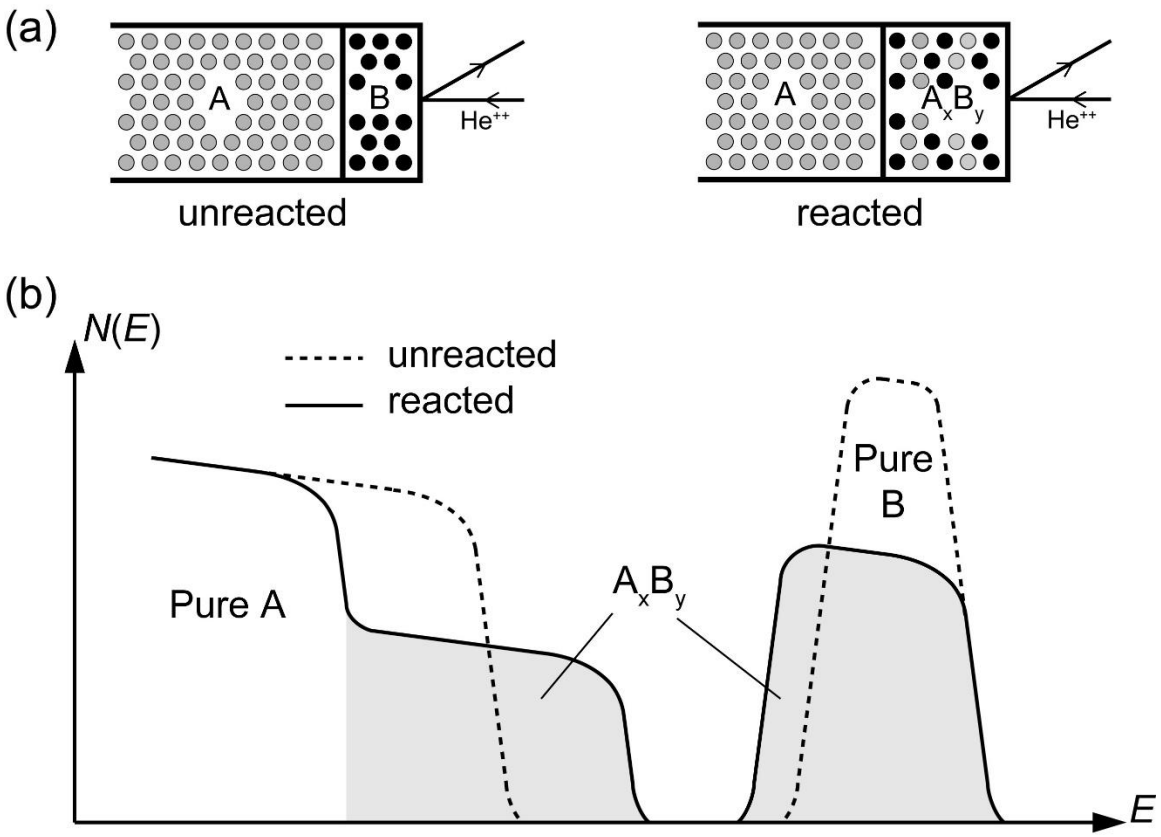

Figure 2.9. Schematic drawing of (a) the He^{++} ions backscattered by a compound A_xB_y before and after reaction, (b) the corresponding RBS spectra. Adapted from Ref. 24.

2.5 Cathodoluminescence (CL)

Luminescence in semiconductor happens when an electron in the conduction band recombines with a hole in the valence band. The energy of the photon depends on the bandgap energy. The energy is also affected by the impurities and defects in the material, which create different recombination paths, as shown in Figure 2.10.

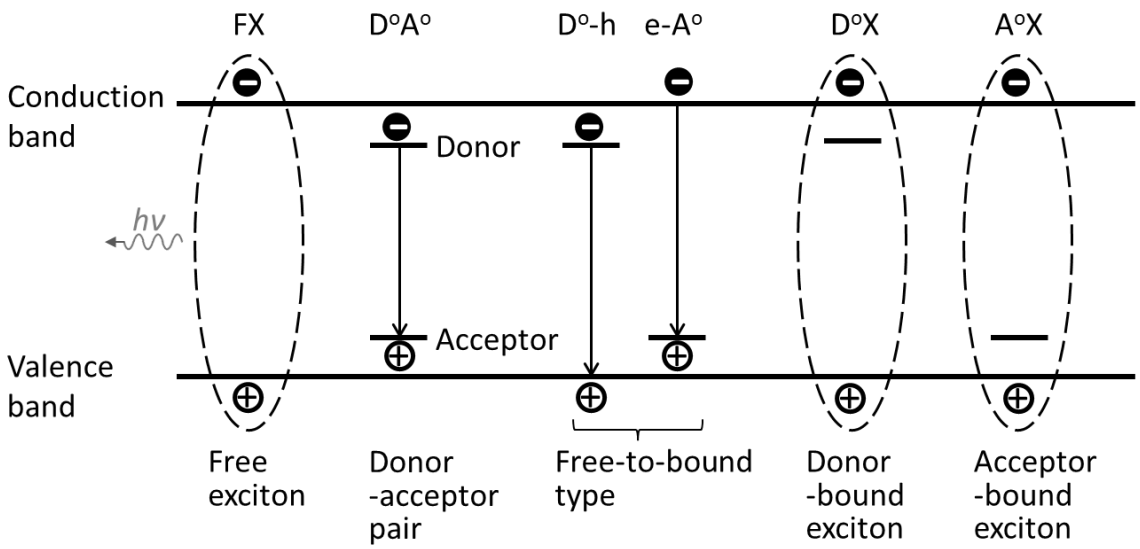

Figure 2.10. Different recombination paths in semiconductors.

In CL, a high-energy electron beam is used to excite the electron from the valence band into the conduction band. Then the luminescence is dispersed by the spectrometer into monochromatic components, which are recorded into a CL spectrum. CL spectra provide information about bandgap energies, and donor/acceptor levels, which are related to compositions of alloys, impurities, and defects.

CL has several advantages over photoluminescence (PL), where the electrons are excited by a laser beam. The electron energy in CL is much higher than the photon energy of the laser in PL, so the bandgap energy is not limited for the material studied by CL. A CL system can be integrated in a scanning electron microscope, so spatially resolved CL can be performed with a highly focused beam. The electron energy can be varied to achieve various penetration depth, so depth profiles of optical properties can be acquired in CL.

2.6 Density functional theory (DFT)

DFT is a computational quantum mechanical method to investigate the electronic structure of many-body systems, particularly condensed matters. DFT is based on two Hohenberg-Kohn theorems.[25,26] The first theorem demonstrates that the ground state properties of the system are uniquely determined by the density of electrons. It uses functionals of the electron density, and reduces the many-body problem of N electrons with 3N coordinates to three spatial coordinates of the functionals. The second theorem defines an energy functional for the system, and proves that the correct ground state electron density minimizes this energy functional.

DFT has been widely used in solid-state physics since the 1970's and has undergone many improvements. However, it still has difficulties in calculating the bandgaps of semiconductors.

Chapter 3 Crystal Structure and Composition of BAlN Thin Films: Effect of Boron Concentration in the Gas Flow*

3.1 Introduction

The BAlGaN compound semiconductors (B-III-N) are being evaluated as a new alloy system for the next generation of photonic and electronic devices. Incorporating boron into the AlGaN system provides possibilities to further optimize the band gap energy and the lattice parameter, independently of each other, in order to minimize the effects of lattice mismatch. Examples of applications are as follows: BGaN can be lattice-matched to AlN and to SiC substrates.[27] BGaN micro-islands have been used as substrate for GaN overgrowth in order to achieve a low threading dislocation density.[28] High reflectivity deep-ultraviolet distributed Bragg reflectors (DBRs) based on BAlN materials can potentially surpass the performance of conventional AlGaInN DBRs in vertical-cavity surface-emitting lasers.[8] And BGaN thin layers have been introduced in AlGaN/GaN high electron mobility transistors to provide an electrostatic barrier to electrons and to improve the confinement of the 2-dimensional electron gas.[29]

Previous reports indicate that it is difficult to obtain high quality B-III-N alloys over a broad range of B compositions while maintaining good crystallinity and smooth morphology.[30–33] Thermodynamic analysis for $B_xGa_{1-x}N$ and $B_xAl_{1-x}N$, typically grown by metalorganic chemical vapor deposition (MOCVD) at ~ 1000°C, gives a high interaction parameter, which determines the excess free energy of mixing, indicating instability over

* Parts of this chapter have been published as:
S. Wang, X. Li, A. M. Fischer, T. Detchprohm, R. D. Dupuis, and F. A. Ponce, "Crystal structure and composition of BAlN thin films: Effect of boron concentration in the gas flow," J. Cryst. Growth, **475**, 334 (2017)

most of the composition range of the alloy.[34] It's reported that B has solubility limits of x = 0.018 and 0.028 in single-phase BGaN and BAlN, respectively.[9] Columnar growth has been observed in BAlN, with lateral dimensions of the order of 10 nm.[10,35] The difficulty in incorporating B may be associated with the high growth temperatures employed to enhance the surface migration of precursors and the production of undesirable adducts through gas-phase parasitic reactions between NH_3 and triethylboron.[35]

Flow-modulated epitaxy (FME) is a useful method of producing III-V semiconductors, where the supply of group-III and group-V sources are injected alternately into the growth chamber without interruption.[36] In a layer-by-layer growth mechanism, FME causes complete surface coverage of the group-V atoms, thus increasing the diffusion length of group-III atoms. The intermittent supply of III vs V elements suppresses parasitic reactions in the gas phase, thus enhancing the metal incorporation in the film. Recently there were reports on the growth at 910 ^{o}C and 1010 ^{o}C of 100-nm thick single-phase wurtzite BAlN with boron content over 10%.[37]

I present here the results of a systematic study of the boron content and microstructure of $B_xAl_{1-x}N$ films grown by FME at 1010 ^{o}C with B/III gas-flow ratios varying from 0.06 to 0.18. X-ray diffraction (XRD) analyses provide B contents that range from x = 0.026 to 0.085, whereas Rutherford backscattering spectrometry (RBS) provide boron contents close to the corresponding B/III gas-flow ratios. This discrepancy is explained by taking into consideration the microstructure and the spatial variation of the composition, which are obtained using transmission electron microscopy (TEM) and electron energy loss spectroscopy (EELS).

3.2 Experimental

The BAlN films were grown on *c*-plane AlN/sapphire templates at 1010 °C in a Close Coupled Showerhead 3x2" Aixtron vertical reactor by FME using the *valves on/off* method.* The Al, B, and N precursors were trimethylaluminum (TMA), triethylboron (TEB), and NH_3. In order to mitigate parasitic reactions in the vapor phase, a low V/III ratio of 60 was used. The study reported here is based on BAlN films grown with B/III gas-flow ratios of 0.06, 0.12, 0.15, and 0.18. All other growth parameters were the same for these films.

The boron content was estimated by XRD using Cu K_α (λ=0.15406 nm) radiation and a four-crystal monochromator (4 × Ge (220)). The XRD area probed was 1 cm x 1 cm, limited by the mask on the X-ray source. The (0002) BAlN diffraction peak is related to the basal plane separation and is correlated to the boron content by Vegard's law. The correlation here uses experimental lattice constants, c = 0.498 nm for AlN and c = 0.4213 nm for BN,[38] which gives B contents with < 5% relative difference from the calculated values, c = 0.495 nm for AlN and c = 0.4179 nm for BN.[7] In addition, the BAlN alloy composition was also estimated by RBS using a 2 MeV He^{++} ion beam, from an area probe of ~ 1.5 mm in diameter.† The typical depth probe is about 1.5 μm. The detection sensitivity in RBS is poor for low-atomic-number elements. For this reason, the B content was derived from the RBS measurement of the Al content in the film, under the assumption of stoichiometry between the group III and V elements.

* The BAlN samples were grown by X. Li, T. Detchprohm, and R. D. Dupuis, at the Center for Compound Semiconductors and School of Electrical and Computer Engineering, Georgia Institute of Technology.

† The RBS measurements were performed by Dr. Barry Wilkens, at Arizona State University. It is understood that a 4 MeV He^{++} ion beam may provide better boron sensitivity.

Cross-sectional TEM samples were prepared by mechanical wedge-polishing and ion milling with an Ar+ beam with 4.0 keV energy. Images were taken in a Philips CM-200 instrument, operated at 200 keV. EELS mapping was performed on the BAlN film with the highest B/III gas-flow ratio of 0.18, using a NION UltraSTEM 100 instrument, operated at 100 keV.

3.3 Results

My study focuses on the evolution of the microstructure with boron content as determined by the B/III gas-flow ratio. The microstructures of the films present a high density of structural defects that affects the ability to accurately measure the boron content.

3.3.1 Measuring the boron content by XRD and RBS

The surface morphology of the films was relatively smooth, with a RMS surface roughness of about 2 nm.[37] Figure 3.1and Table 3.1 summarize the boron content in the four films, estimated from measurements by XRD and RBS. Notice that the boron content measured by RBS is found to be larger than when measured by XRD. In XRD, the diffraction intensity is plotted along a $\theta/2\theta$ scan; the patterns corresponding to the films are shown in Figure 3.2. The XRD patterns consist of two peaks, one is centered at 18.016^{o} and corresponds to the (0002) AlN reflection, and the other is a broader peak centered at a slightly higher angle and corresponds to the (0002) BAlN reflection. For example, the pattern for B/III = 0.12 presents a peak centered at 18.183^{o} that correspond to a boron composition x = 0.059. The full-width-at-half-maximum (FWHM) of the BAlN peak is 0.11^{o}. There are several ways to interpret the FWHM: (a) It is due to a boron composition variation; (b) it is due to defects and strain; and (c) it is due to particle-size broadening.

The last one is most likely to be the case. The broadening due to film thickness can be estimated from Scherrer equation $B(2\theta) = \frac{K\lambda}{Lcos\theta}$.[22] With $K \approx 1$, crystal size L = 45 nm, λ= 0.154 nm, the broadening is expected to be 0.0018 rad or 0.1° for θ near 18°, which is similar to the observed value of 0.11 °.

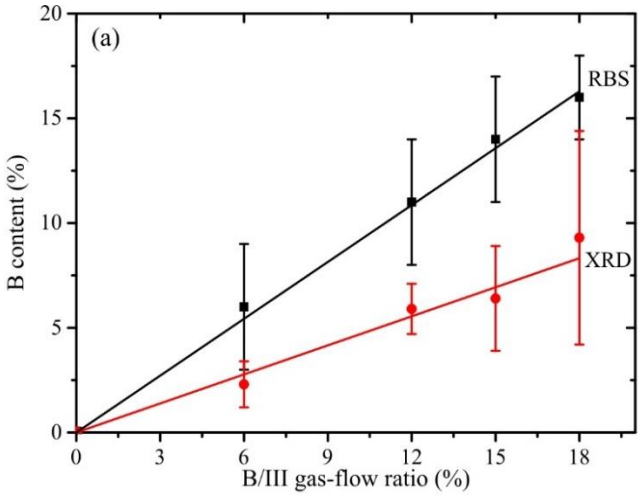

Figure 3.1. Boron content in the film as a function of the B/III gas-flow ratio in the gas flow, determined by XRD (circles) and by RBS (squares), with corresponding linear fits.

Table 3.1. Boron content in the gas flow during growth, and in the thin film measured by XRD and RBS. Other growth parameters are kept constant: the growth temperature is 1010 °C, the V/III gas source ratio is 60, the TEB + TMA flow is 57 μmol/minute, the growth rate is 0.32 nm/s. FME pulse period: TEB + TMA = NH_3 =0.8 s. The film thickness is about 45 nm in all cases.

B/III	XRD		RBS		XRD/RBS
	[B]	Lattice Mismatch (%)	[B]	Lattice Mismatch (%)	
0.06	0.023	0.41	0.06	1.08	0.38
0.12	0.053	0.94	0.11	1.98	0.48
0.15	0.064	1.14	0.14	2.53	0.46
0.18	0.093	1.66	0.16	2.88	0.58

The XRD intensity relies on Bragg diffraction from crystal planes that are parallel to the diffraction plane of the diffractometer, which is experimentally determined by alignment of the substrate. Therefore, regions in the BAlN film that are not parallel to the substrate will not contribute significantly to the measured XRD intensity in the $\theta/2\theta$ scan. Note that the BAlN peak is much weaker (3 to 5 orders of magnitude) than the AlN peak, making reciprocal space maps not very useful.[37]

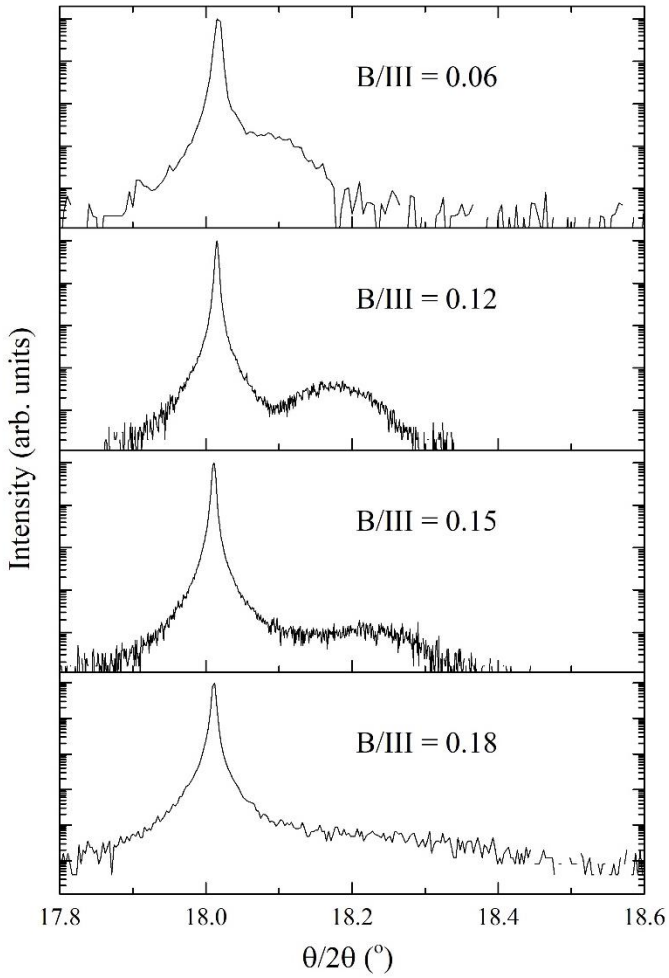

Figure 3.2. XRD θ-2θ scan of the (0002) plane for the thin films.

Composition determination by RBS is achieved by measuring the backscattering of a beam of alpha particles. The recoil energy of the backscattered particles depends on the atomic weight of the individual atomic constituent, according to an elastic collision where kinetic energy is conserved. The measured energy is also affected by the distance of the scattering atoms to the surface of the material, since some energy is dissipated by friction from the inelastic scattering between the alpha particle and the material. In this manner, the RBS technique allows the measurement of the average composition as a function of depth of the scattering atoms. The scattering cross section, which determines the yield, is proportional to Z^2 (Z = atomic number). Therefore, RBS is more sensitive for large atoms, and has a lower detectability for smaller atoms like boron. RBS is also sensitive to the thin film morphology, and thus the columnar growth in the materials provides a challenge.[39] The sum of these issues makes for a large uncertainty in the composition determination by RBS. An example of the RBS measurements for a BAlN film with B/III gas-flow ratio of 0.18 is in Figure 3.3, which shows the RBS data and a simulation (smooth line) using XRUMP software.[40] The Al content, calculated by fitting the step in the data near the Al onset, corresponds to 0.84. The boron content is calculated by taking the difference [B] = 1 - [Al] = 0.16. Here I assume that the drop in Al content is due to B atoms substituting Al atoms, and that there are no interstitial B atoms.

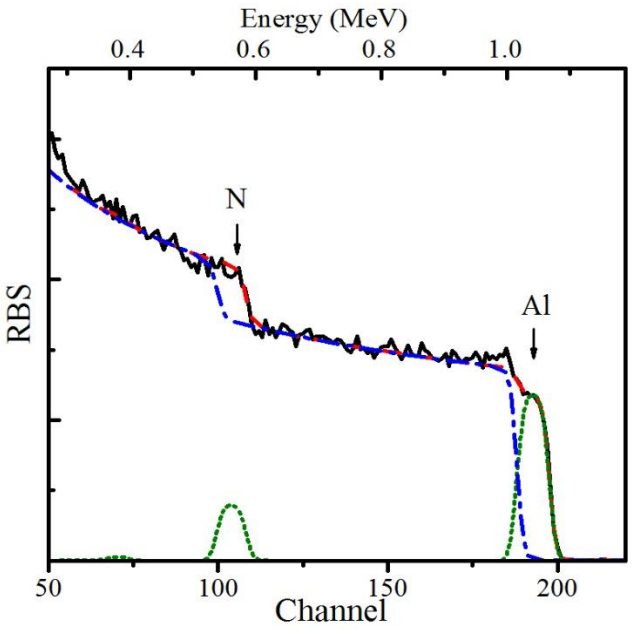

Figure 3.3. RBS spectrum for the thin film with B/III = 0.18. The green dotted line and the blue dash-dotted line are the simulations for the BAlN layer and AlN template, respectively. The red dashed line is the sum of the two layers.

3.3.2 Evolution of the microstructure of BAlN alloys with increasing B/III gas-flow ratio

Figure 3.4 shows a cross-sectional TEM image of the $B_xAl_{1-x}N$ film with B/III gas-flow ratio of 0.06 (x = 0.06 by RBS and 0.023 by XRD). The film exhibits columnar structures with a lateral dimension of ~ 10 nm. The inset in Figure 3.4 is a fast Fourier-transform (FFT) diffractogram, corresponding to the region in the TEM image indicated by a box, and shows only a wurtzite structure. The BAlN film in Figure 3.5 grown with a B/III gas-flow ratio of 0.12 (x = 0.11 by RBS and 0.059 by XRD), shows irregular domain boundaries, without noticeable change in the crystal orientation and structure in the FFT pattern (inset).

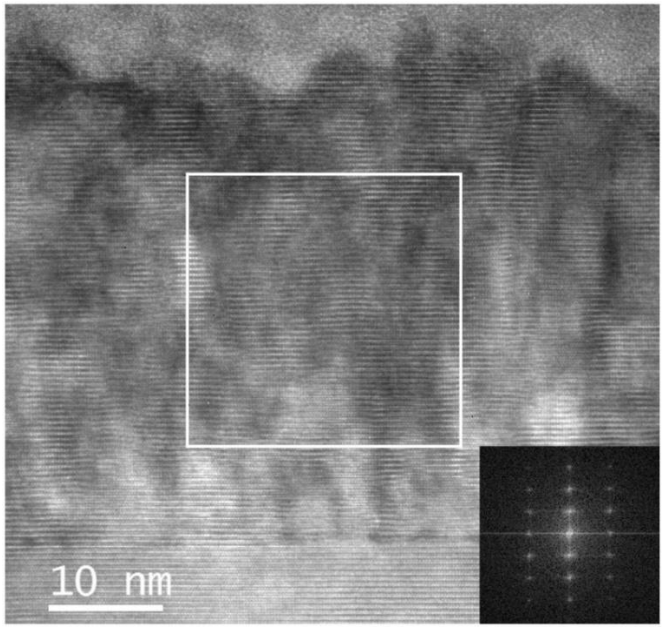

Figure 3.4. Microstructure of the BAlN/AlN film grown with a B/III gas-flow ratio of 0.06. Cross-section on-axis multi-beam TEM image along the $[11\bar{2}0]$ AlN projection. The film is ~ 45 nm thick and presents a rough surface corresponding to a columnar structure with columns of 10 nm diameter. FFT diffractogram of the region in the box indicates the sole presence of a wurtzite structure.

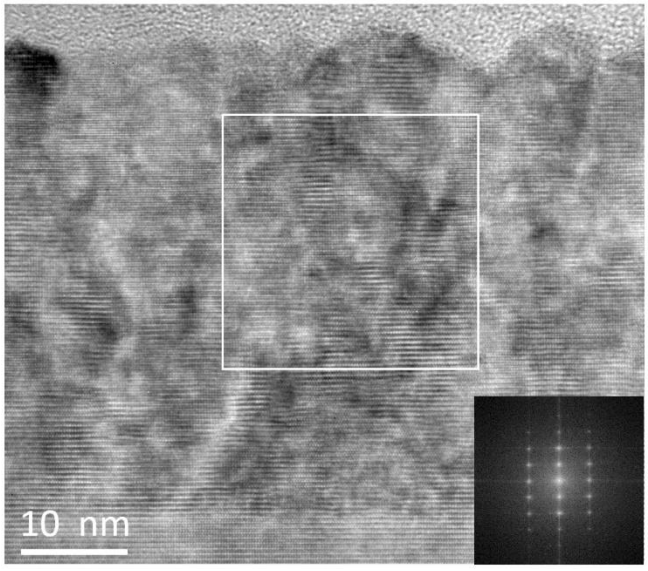

Figure 3.5. Microstructure of the BAlN film grown with a B/III gas-flow ratio of 0.12. Cross-section on-axis multi-beam TEM image along the $[11\bar{2}0]$ AlN projection. The film thickness is ~45 nm. FFT diffractogram of the region in the box indicating a wurtzite structure.

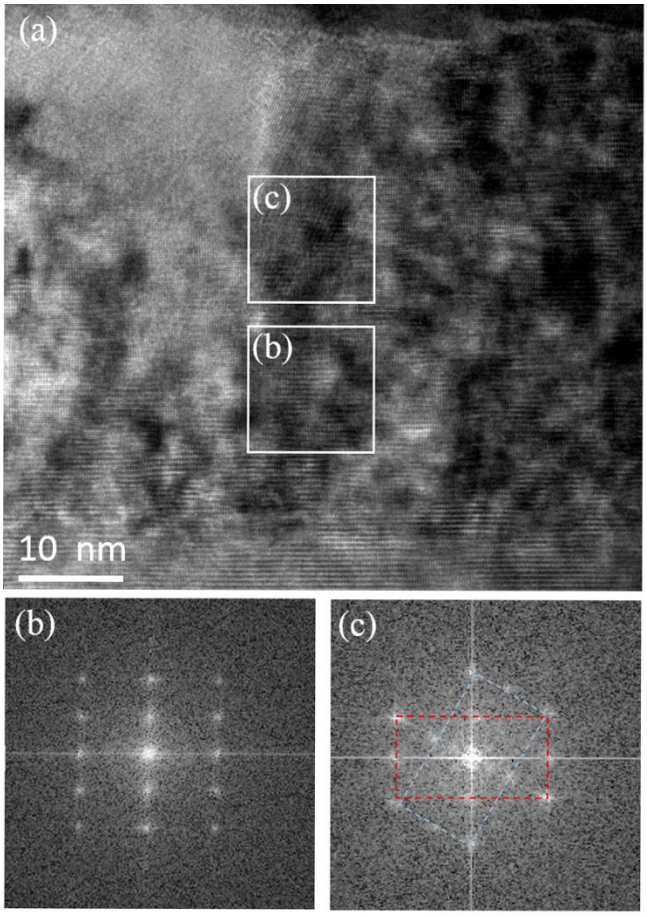

Figure 3.6. Microstructure of BAlN/AlN film grown with a B/III gas-flow ratio of 0.15. (a) Cross-section on-axis multi-beam TEM image along the $[11\bar{2}0]$ AlN projection. The film thickness is about 45 nm. FFT diffractograms of the region in the boxes indicate (b) bulk wurtzite BAlN and (c) wurtzite structure rotated by about 60°.

As the boron content is further increased, twin formation is observed in Figure 3.6(a) for films grown with a B/III gas-flow ratio of 0.15 (x = 0.14 by RBS and 0.064 by XRD). The bottom region, depicted by the lower box, shows good epitaxy with the *c*-plane parallel to the substrate, as evidenced by the FFT in Figure 3.6(b). The FFT pattern in Figure 3.6(c), corresponding to the upper box in the TEM image, shows two overlapping crystal structures that result from a twin formation. The extra lattice planes seen in the upper box are (0002) planes tilted by ~60°.

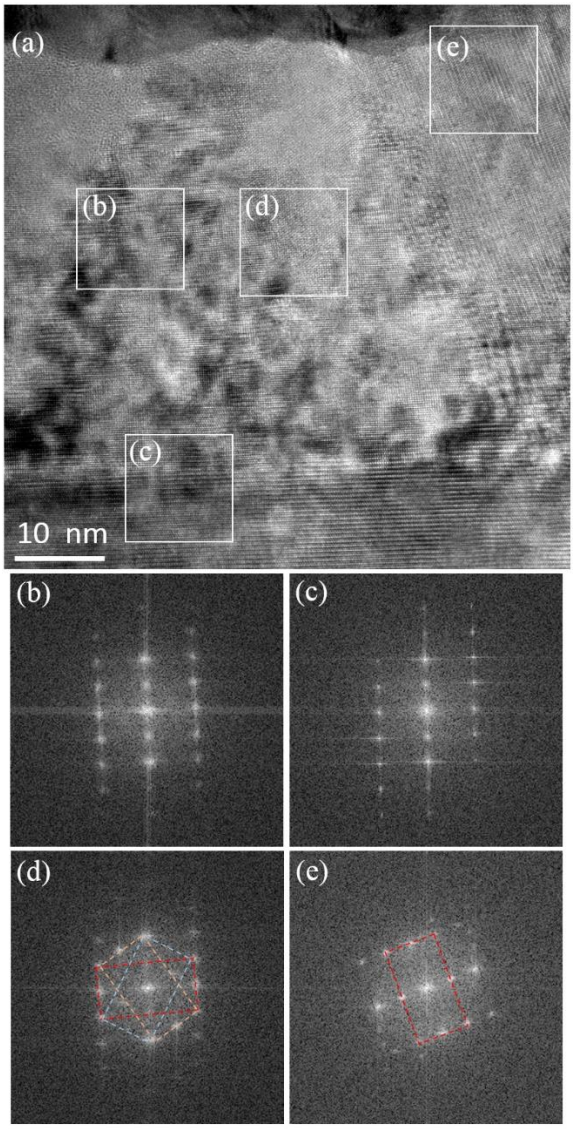

Figure 3.7. Microstructure of BAlN/AlN film grown with a B/III gas-flow ratio of 0.18. (a) Cross-section on-axis multi-beam TEM image along the $[11\bar{2}0]$ AlN projection. (b) FFT diffractogram of the BAlN structure with the same orientation as (c) AlN substrate. (d) and (e) FFT diffractogram showing twins.

The BAlN film with B/III gas-flow ratio of 0.18 (x = 0.16 by RBS and 0.093 by XRD), shown in the TEM image in Figure 3.7(a), exhibits a higher number of twin boundaries than in films with B/III gas-flow ratios < 0.15. The region labeled (b) in the image has the same orientation as the AlN underlayer, labeled (c) as observed in the

respective FFT patterns in Figure 3.7(b,c). In a similar manner, the region labeled (d) contains two twin boundaries tilted by ~ 60^{o}, one clockwise and other counter-clockwise, with respect to region parallel to the substrate, also observed in the FFT pattern. Figure 3.7(e) shows the diffraction pattern of a region corresponding to a single twin, rotated clockwise.

3.3.3 Twin formation

For B/III gas-flow ratios ≥ 0.15 (Figure 3.6(c) and Figure 3.7(d,e)), I observe the formation of twins. They are observed as extra spots in the diffraction patterns that result from a mirror reflection about certain lattice planes. The relationship between the $[11\bar{2}0]$ reciprocal lattice projection and two possible twin planes is shown in Figure 3.8, corresponding to reflections about $\{1\bar{1}01\}$ and $\{1\bar{1}03\}$ lattice planes in real space. Enlarged versions of Figure 3.7(d) and Figure 3.6(c) are shown for comparison with diagrams of the projection of the reciprocal lattice and its twins. Both twinning systems give similar patterns, so I cannot distinguish them from the diffraction patterns. Similar twinning structures have been reported for wurtzite GaN nanostructures.[41,42] It has been reported that the $\{1\bar{1}03\}$ twin planes are energetically preferred in nanowires,[43] but I cannot eliminate the possibility of $\{1\bar{1}01\}$ twin planes in the BAlN thin films.

It is important to note that twinned regions in the film will not contribute to the XRD intensity in $\theta/2\theta$ scans, since their basal planes will not be parallel to the substrate.

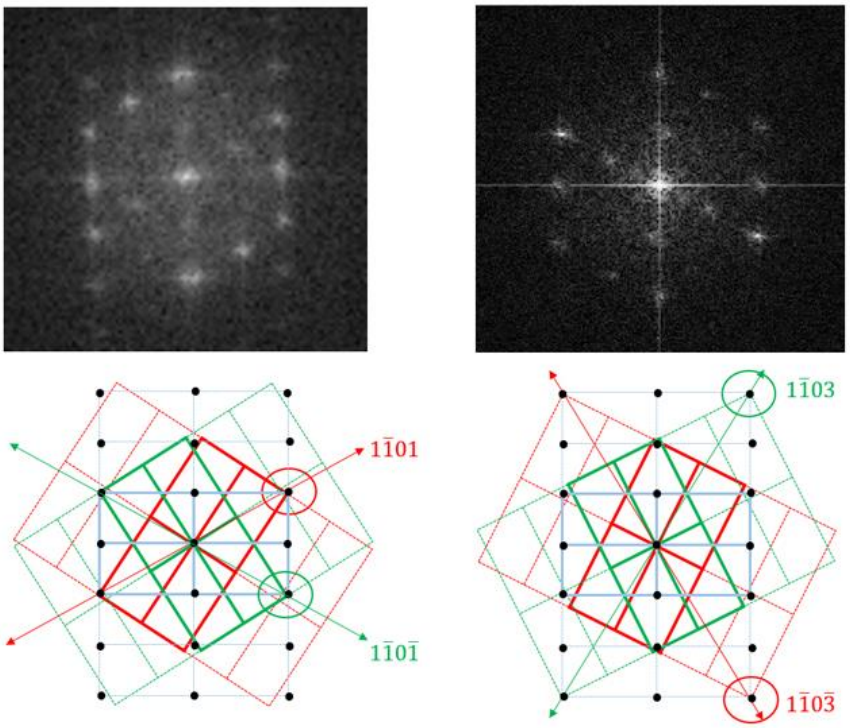

Figure 3.8. Diffraction patterns corresponding to twinning in BAlN thin films with B/III gas-flow ratio of (a) 0.18 and (b) 0.15. Schematic diffraction pattern of the twinned BAlN (red and green) and the bulk material (blue) for twinning about (c) $\{1\bar{1}01\}$ and (d) $\{1\bar{1}03\}$ lattice planes in real space. The two diagrams are too similar for accurate experimental identification in the present work.

3.3.4 Spatial composition variations

The spatial composition variation has been probed using EELS in the TEM. The spectral regions corresponding to the Al *L*-edge, B *K*-edge, and N *K*-edge with the background removed for the film with B/III gas-flow ratio of 0.18 is shown in Figure 3.9. The spectra of Al and N closely follow those for slightly oxidized AlN.[44] The uniform spatial distribution of N in Figure 3.9(c) indicates a uniform thickness (and density) of the TEM foil. By comparing the concentration of Al and B in Figure 3.9(d) and (e), I observe that the two elements have complementary distribution, especially in the encircled region.

Only the epitaxial portion outside this region in Figure 3.9(e), which has less boron, is expected to contribute to the B content measured by XRD.

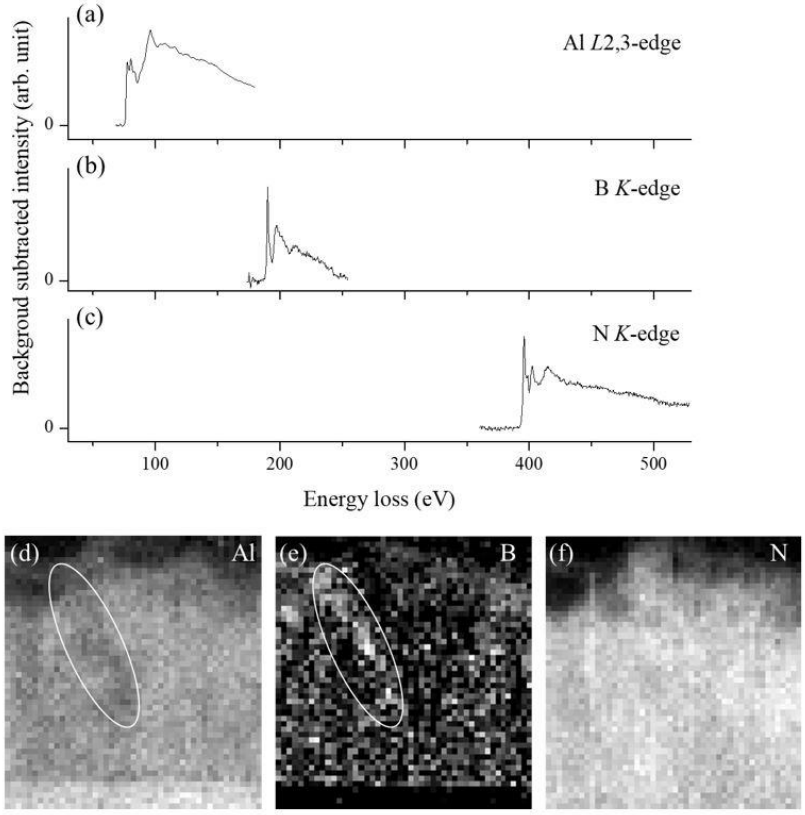

Figure 3.9. EELS spectra showing the (a) Al *L*-edge, (b) B *K*-edge, and (c) N *K*-edge after background subtraction, and the corresponding compositional mapping of these elements. The circle shows a region of relatively higher boron and lower aluminum content.

3.4 Discussion

3.4.1 Absence of phase separation in BAlN alloys

The boron solubility was predicted from the interaction parameter to be x = 0.028 for $B_xAl_{1-x}N$ and y = 0.018 for $B_yGa_{1-y}N$.[9] In this study, relatively sharp XRD peaks (Figure 3.2) were observed corresponding to a boron content up to x = 0.059, and broader peaks were observed indicating boron contents up to x = 0.093. As described in a previous section,

these boron content values correspond to regions of the film with basal planes parallel to the AlN underlayer, and therefore are evidence of uniform boron incorporation on the planes parallel to AlN. I have looked at other regions of the XRD spectra for evidence of regions of higher boron content, which would result from phase separation, but failed to obtain such evidence. I therefore believe that for this growth technique there is no phase separation of the spinodal type.

The crystal defect structures of the thin films present interesting characteristics. Analysis of the TEM images show the presence of the wurtzite structure throughout all regions studied – no other phases in electron diffraction patterns have been observed. Stacking faults and other disorders in the stacking sequence are not observed, as their presence would result in streaks along the *c*-direction in the FFT patterns. No phase separation is observed in the BAlN/AlN layers. I attribute this to the fact that B atoms are smaller than Al, giving rise to local tensile stress. InGaN alloys are different in that In is larger than Ga, causing compressive strain in InGaN/GaN, with predicted spinodal decomposition.[45] However, under strain-relaxed conditions, high-indium-content InGaN epilayers have been reported without evidence of spinodal decomposition.[46]

3.4.2 Epitaxial growth vs boron incorporation in BAlN alloys

As mentioned above, the proportion of epitaxial growth parallel to the substrate appears to increase linearly with B/III gas-flow ratio, up to a maximum boron concentration of $x = 0.093$ measured by XRD in this work. On the other hand, RBS measurements suggest that the efficiency of boron incorporation appears to closely follow the gas-flow ratio up a maximum boron concentration of $x \approx 0.16$. Following the discussion above, the

difference in the boron concentration by XRD and RBS can be explained based on the nature of the measurements. XRD is providing information about regions of parallel epitaxy, while RBS is about the average concentration based on measurement of Al backscattering and III-N stoichiometric considerations. The fact that $\theta/2\theta$ XRD scans do not provide information about regions with basal planes with a non-parallel orientation to the substrate, suggests that those regions may contain the excess boron suggested by the RBS data. Those regions consist of intergranular regions and twins. The spatial compositional variations in Figure 3.9 suggest boron segregation at the columnar boundaries. Attempts to accurately measure the composition by EELS have not been successful because of the small probe volumes and the lack of standards for EELS regarding B in BAlN.

3.4.3 Growth mechanisms and microstructure

The columnar microstructure in Figure 3.4 and Figure 3.5 suggest that the early stages of thin film growth involve island formation of the Volmer-Weber or Stranski-Krastanov types. Tendency towards island formation in the early stages of growth of nitride semiconductors has been reported in the literature for epitaxial growth of GaN on sapphire and on AlN,[47,48] and for $B_xGa_{1-x}N$ on GaN and on AlN.[2] Columnar growth has been reported for $B_xAl_{1-x}N$ thin films grown by FME-MOCVD with x~0.015,[10] and more recently with x = 0.12.[11,13] I therefore speculate from the TEM observations that for low boron content, well-defined and stable columns result from island growth in the early stages of epitaxy. The surface roughness is related to the columnar lateral dimensions. This is observed in Figure 3.4, for growth with B/III gas-flow ratio = 0.06, where the

columnar diameter (~ 10 nm) is similar to the surface roughness period. For higher boron contents, the columnar diameters tend to be smaller, and the columns are not always normal to the substrate. The lattice planes appear to follow the orientation of the substrate even when the columns are inclined. The finer columns tend to coalesce and form smoother growth fronts, as observed in Figure 3.5 (for B/III gas-flow ratio = 0.12). The dark regions in the TEM images are attributed to strong diffraction from regions with good alignment of the crystal zone axis with respect to the electron beam. The FFT patterns displayed as insets in the TEM images indicate that the c-axis of the columnar structure aligns well with the growth direction, i.e. it is a well-aligned epitaxial film.

3.5 Summary and Conclusions

I have analyzed the microstructure and composition of thick BAlN films with B/III gas-flow ratios ranging from 0.06 to 0.18. For low boron contents, a columnar structure reflects island formation in the early stages of growth. The columnar diameter decreases with boron content. No tilt in the orientation of the columns was observed from diffraction patterns. Twinned regions are observed at B/III gas flow ratios at and above 0.15, ~10 nm in diameter. The B content obtained by RBS closely follows the B/III gas-flow ratio, indicating high efficiency of boron incorporated into the film. The B content measured by XRD is noticeably less than measured by RBS. Given that $\theta/2\theta$ XRD spectra are sensitive only to crystal regions that are parallel to the substrate, and in the absence of tilted regions, we attribute this difference to possible boron segregation at the columnar boundaries and other crystalline defects such as twinned regions. No evidence of phase separation has been observed in the films.

Chapter 4 Identification of Point Defect Energies in BAlN Using High-Resolution Electron Energy Loss Spectroscopy

4.1 Introduction

In the previous chapter, I reached the conclusion that there could be boron segregation at the planar defects in the BAlN thin films. However, the exact nature of the excess boron remains unresolved. It is possible that this portion of boron forms boron interstitials, a kind of point defect in the films. It would be interesting to identify the point defects and correlate them with the growth conditions.

Density functional theory (DFT) calculations can be a useful tool to investigate properties of III-nitride semiconductors. The native point defects and impurities in AlN have been studied to provide their electronic structure, atomic configurations, and formation energies.[49] However, the properties of B related defects have not been revealed. Recently, DFT calculations have been done on perfect BAlN films with different B composition[7]. It will be interesting to perform DFT on BAlN films with defects.

The low-loss region of EELS contains electronic information from conduction and valence-band electrons.[14] It has been used to characterize the states in the bandgap related to defects.[50,51] So, low-loss EELS can be used here to experimentally observe the boron related point defects in the films.

In this chapter, I studied two BAlN thin films discussed in Chapter 3, with gas-flow B/(B+Al) ratio as 0.12 and 0.18, respectively. I observed features with energy ranging from 0.2 to 0.8 eV in EELS low-loss spectra. The features were identified by comparing to the

DFT calculations performed on AlN crystal, as well as on possible point defects in the BAlN film.

4.2 Experimental method

The BAlN films are grown by MOCVD, with gas-flow B/(B+Al) ratio of 0.12 and 0.18. The detailed growth process is described elsewhere.[37] The HAADF images are acquired at 100kV in the NION HERMESTM 100 with a beam convergence of 30 mrad using the aberration corrector. The low-loss EELS spectra are taken at a lower acceleration voltage of 60 kV, which is needed to suppress the background in the bandgap region caused by Cerenkov radiation.*

4.3 Results and discussion

Figure 4.1 shows the atomic-resolution HAADF image near the BAlN/AlN interface, where the film is grown with gas-flow B/(B+Al) ratio of 0.12. The BAlN region appears less homogenous than the AlN region. The darker regions have higher boron concentration, because the contrast of HAADF image is proportional to Z^{α} (Z is atomic number, α varies between 1.2 and 1.8, depending on the collection angle).[52] The undulating contrast of the BAlN region indicates inhomogeneity of B distribution, which we hypothesized were due to point defects.

* The HAADF images and EELS spectra were taken by Dr. Katia March, at Eyring Materials Center, Arizona State University

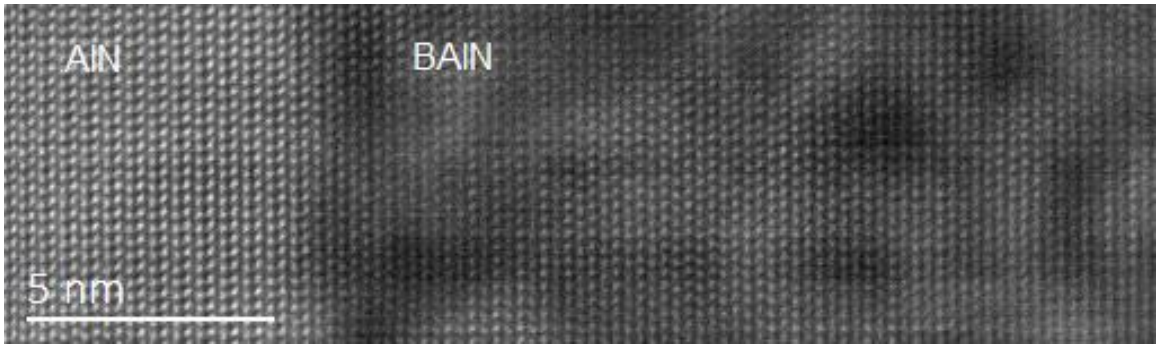

Figure 4.1. HAADF image showing AlN and boron implanted region, with B/(B+Al) = 0.12.

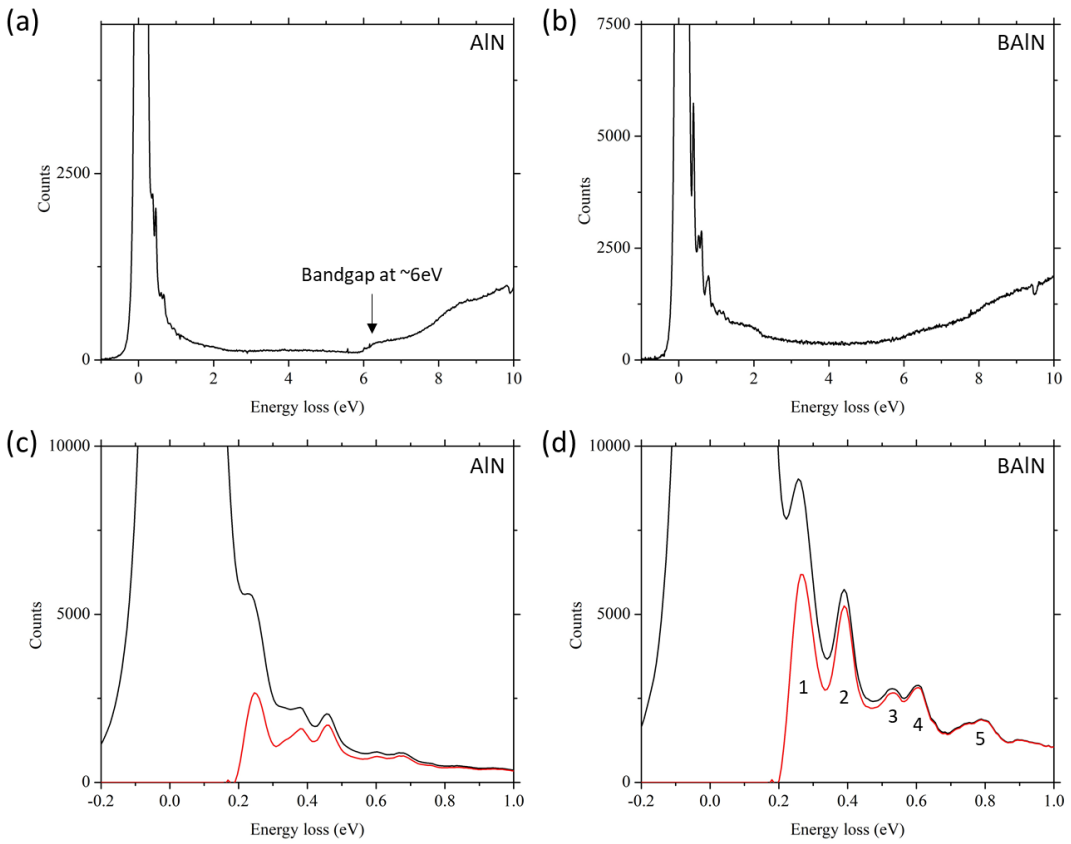

Figure 4.2. (a) and (b) EELS low-loss spectra in the AlN substrate and BAlN film with B/(B+Al) = 0.18, respectively. (c) and (d) Magnified spectra in the energy range below 1 eV. The red lines show the spectra after background subtraction. The features in BAlN spectrum are numbered from 1 to 5, and summarized in Table 4.1.

To study the properties of the point defects, EELS low-loss spectra are taken and compared in the AlN substrate and in the dark regions of BAlN film with B/(B+Al) = 0.18, as shown in Figure 4.2. The bandgap of AlN is ~6 eV, which is shown as a step in Figure 4.2(a). This result is consistent with the accepted value of 6.0 eV.[53] In comparison, the band-edge emission of BAlN doesn't give a clear step in Figure 4.2(b), which may be related to a band tail in the conduction band. Figure 4.2(c) and (d) shows the region below 1eV for AlN and BAlN respectively. The spectrum in Figure 4.2(d) exhibits higher and more peaks than Figure 4.2(c). These peaks are summarized in Table 4.1, and will be discussed in the next section. The AlN substrate should contain only very low-level density of defects, considering the uniformity in Figure 4.1. The peaks in the spectrum for AlN substrate should be B-related signals, due to the delocalization of the defect states, considering the spectrum was taken in an AlN region ~10 nm from the interface.

Table 4.1. Summary of low-energy features in the BAlN EELS spectrum.

Peak #	Energy (eV)	Possible defect	Transition
1	0.27	N vacancy	F → G
2	0.39	Al interstitial	E → CBM
3	0.53	Not assigned	
4	0.60	Al interstitial	D → E
5	0.79	B interstitial	B → CBM
		N vacancy	G → CBM

The peaks are assigned to defects according to the relative positions of valence band maximum (VBM), conduction band minimum (CBM), and defect states summarized in Table 4.2.

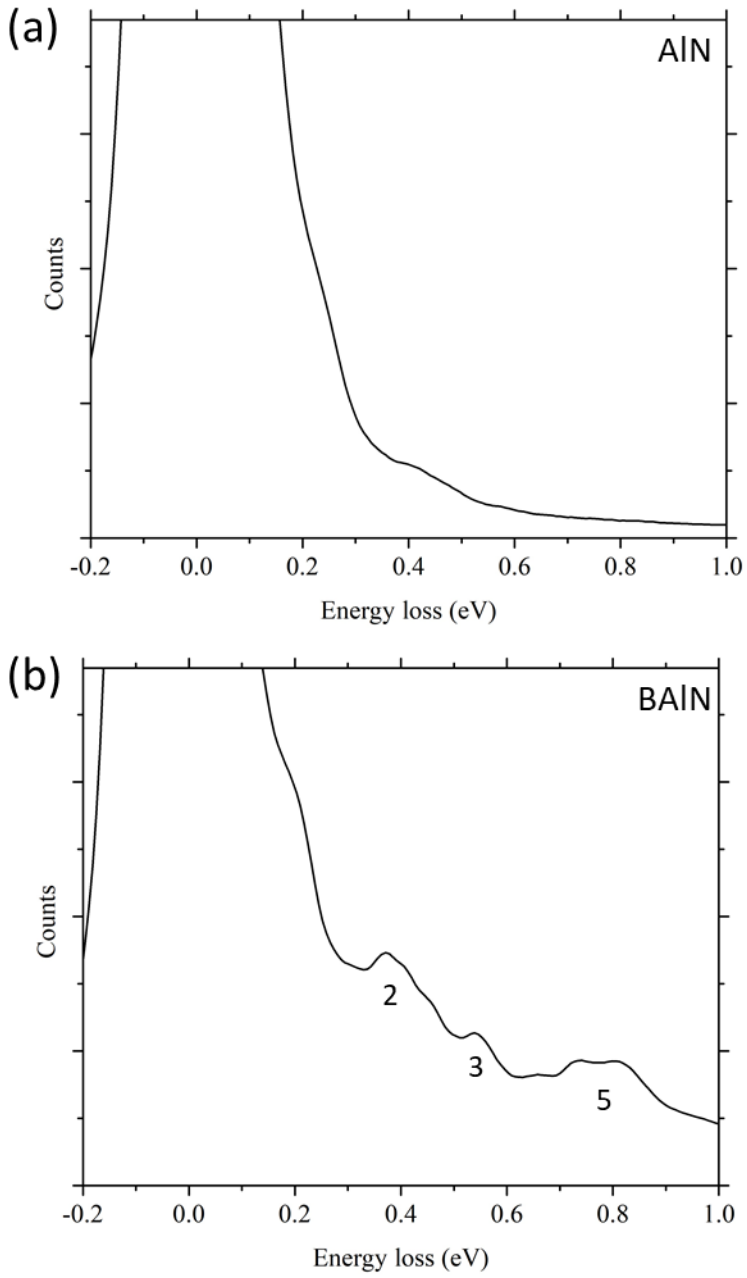

Figure 4.3. EELS low-loss spectra in the energy range below 1 eV of (a) AlN and (b) BAlN film with B/(B+Al) = 0.12. The numbers in (b) are in the same fashion of Figure 4.2(d).

For comparison, similar analysis is carried out on the less defective BAlN film with B/(B+Al) = 0.12, as shown in Figure 4.3. In Figure 4.3(a), the spectrum of the AlN region exhibit very low level of defect peaks, indicating minimum effect of delocalization and low density of defects in the BAlN film. In Figure 4.3(b), the spectrum also shows three peaks labeled 2, 3, and 5 from the spectrum of the more defective sample in Figure 4.2(d). The relative intensity of No. 2 is lower in Figure 4.3(b), while No. 3 and 5 are about the same levels in the two samples. No new peaks emerge in Figure 4.3(b).

Next, DFT is used to explore whether postulated point defects give rise to states in the band gap, and whether transitions involving these states match experimental observations.[*] If a state in the band gap is unoccupied, the EELS spectrum will show a threshold corresponding to the transitions from the top of the valence band, followed by a slow decrease due to excitation of electrons at lower energies in the valence band. A similar argument applies to occupied band gap states. In this case the threshold corresponds to a transition to the lowest level in the conduction band. The slow decrease at higher energies arises from exciting electrons from the filled band gap state to higher energy states in the conduction band.

[*] The DFT calculations were performed by Dr. Peter Rez, at Department of Physics, Arizona State University.

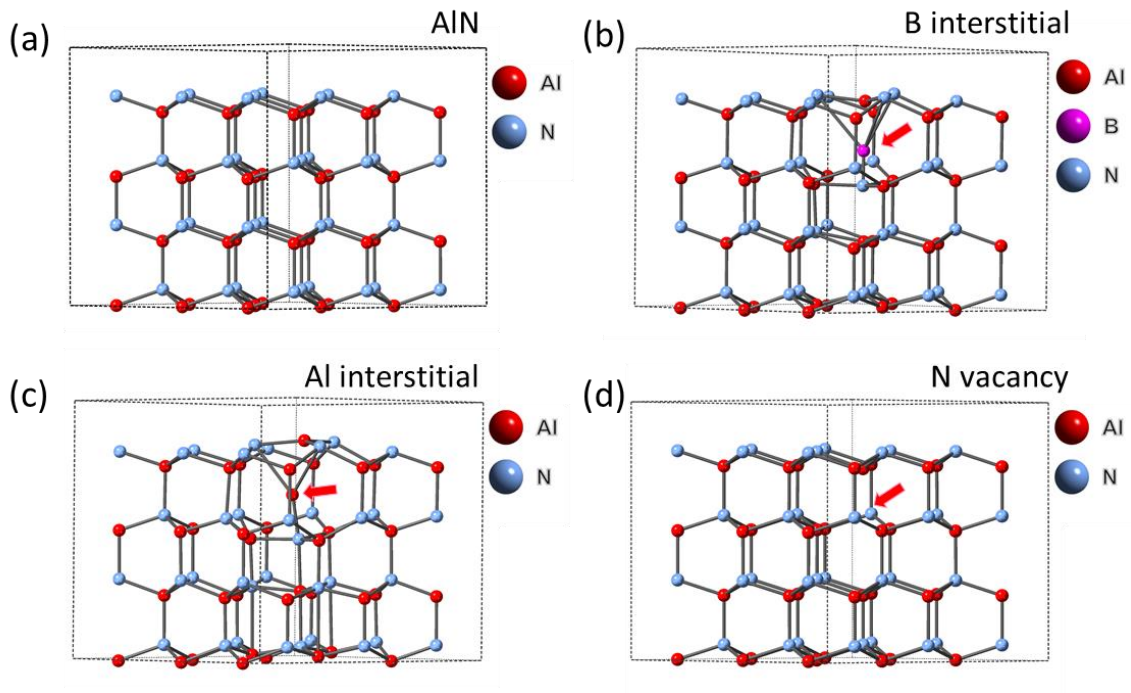

Figure 4.4. Supercell structures used in DFT calculations. (a) 3x3x2 AlN unit cells. (b) With single B interstitial. (c) With single Al interstitial. (d) With single N vacancy. The point defects structures in (b)-(d) are relaxed from (a) using 3x3x3 k-points. The arrows mark the position of the defects.

VASP DFT calculations were performed using local density approximation and the projection augmented-wave method,[54,55] for single Al, B and N interstitial atoms, single Al and N vacancies in a supercell constructed from 3x3x2 AlN unit cells. The structures were initially relaxed with 3x3x3 k points, and then a high-resolution density of states (DOS) was calculated with 5x5x5 k points. The supercells are shown in Figure 4.4.

The bandgap for AlN from the DOS shown in Figure 4.5(a) is underestimated as 4.6 eV, as is typical for DFT. Despite this limitation DFT can identify when a particular defect will give energy levels in the band gap, and is generally reliable for showing the order of energy levels. Figure 4.5(b) to (d) show the evidence of defect states inside the bandgap, which is summarized in Table 4.2. The calculations also determined the position of the

Fermi level shown as 0.0 eV, so plausible transitions to the empty states in the conduction band could be identified.

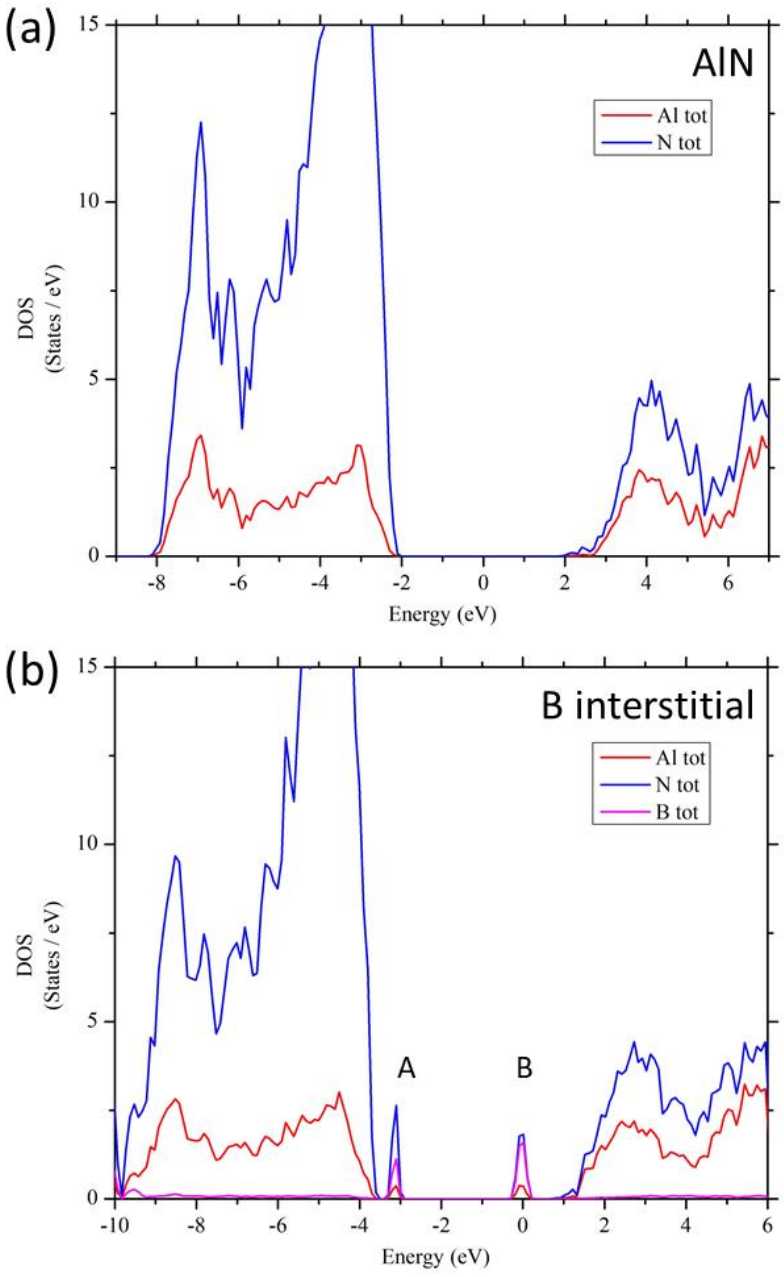

Figure 4.5. (Continued next page)

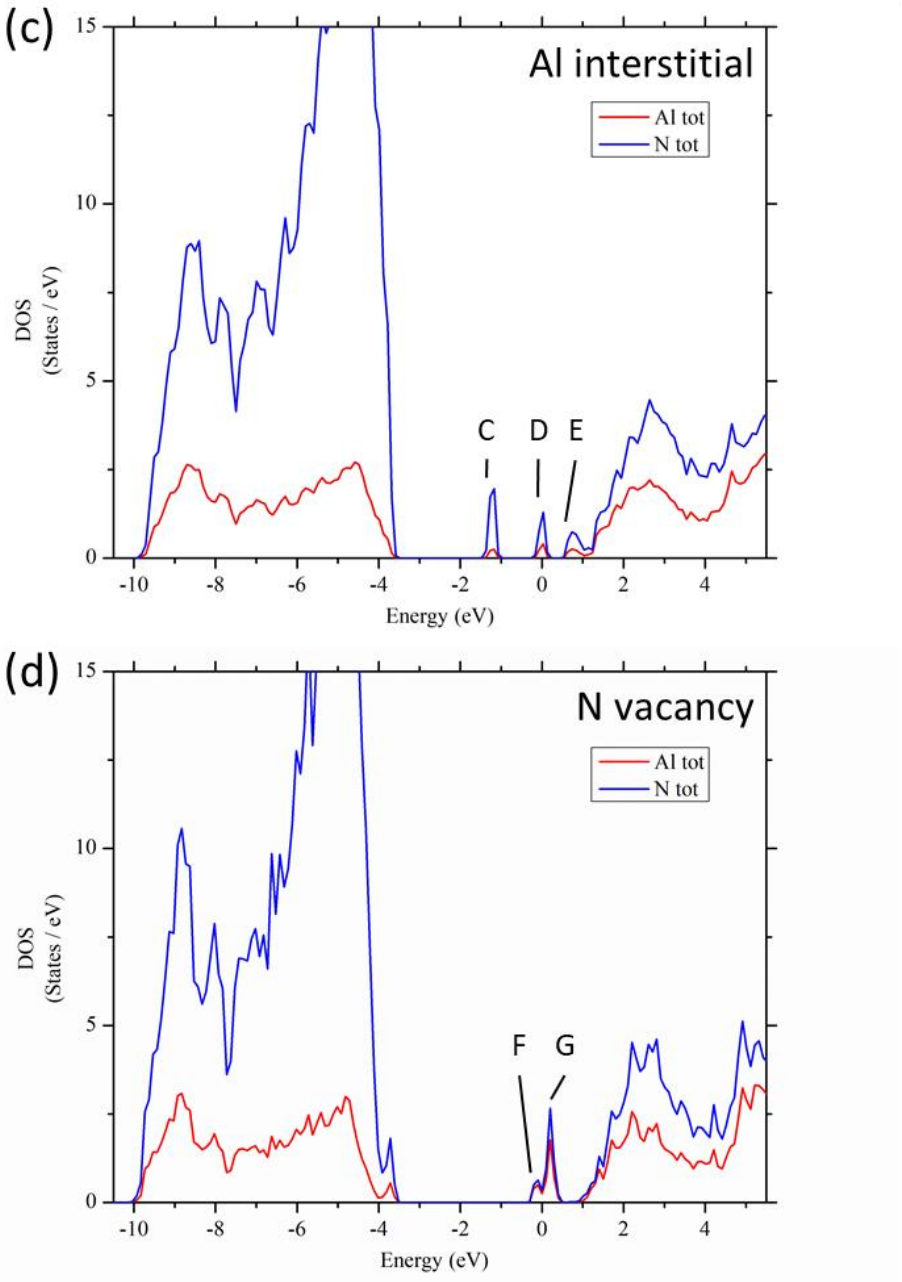

Figure 4.5. DFT calculations for (a) AlN in 3x3x2 supercell, (b) with single B interstitial, (c) with single Al interstitial, and (d) with single N vacancy. The defect states in the bandgap are marked from A to G, and are summarized in Table 4.2.

Then the peaks in Table 4.1 are compared with the possible transitions between the defect states, VBM, and CBM. If there is an approximate match, the peak can be correlated

to certain type of point defects, as described in Table 4.1. Here, most of the peaks in low-loss EELS spectrum can be assigned, indicating the domination of point defects in the IR emission less than 1 eV.

Table 4.2. Summary of defect states calculated by DFT.

Point defect	Defect states			Fermi level
B interstitial	A	B		3.5
	0.4	3.5		
Al interstitial	C	D	E	3.5
	2.3	3.5	4.2	
N vacancy	F	G		3.5
	3.4	3.7		

Each state shows its energy (in eV) above the VBM. Only the states allowing transitions are taken into consideration when assigning the peaks.

Combining the EELS spectra and DFT simulations, the results can be interpreted as follows: The density of B interstitials, represented by the peak height of No. 5, doesn't increase significantly as the B/(B+Al) ratio increase from 0.12 to 0.18. One reason may be the qualitative nature of this experiment. The solubility limit of B in AlN is reported as 2.8%,[9] and both samples are attempting to introduce a B composition higher than that limit. With the assumption that all the excess B should go to interstitial sites, the respective excess amounts of B are 9.2% and 15.2% for the two samples. This difference may not be clearly observed in the peaks. An alternate explanation is to consider the B interstitial density to be the same in the two samples. There may be a maximum allowed density of B interstitials in the films. Any B beyond that limit during growth will tend to segregate at the grain boundaries and twin formations, in non-interstitial forms and creating more defects. This explains why the increase in the gas-flow B/(B+Al) ratio leads to the finer microstructures

discussed in Chapter 3, and to higher density of other species of point defects (Al interstitials and N vacancies) shown in Figure 4.2(d).

4.4 Conclusion

Defect states inside the bandgap of BAlN films have been observed by EELS low-loss spectra. DFT calculations identified the states as the defect states of B and Al interstitials, and N vacancies. The B interstitials may be resulted from introducing a B composition higher than the solubility of B in AlN. The increase in the densities of Al interstitials and N vacancies may be a consequence of the more defective microstructures caused by an increase in the B doping level.

Chapter 5 Dislocation Baskets in Thick $In_xGa_{1-x}N$ Epilayers*

5.1 Introduction

$In_xGa_{1-x}N$ alloys have a direct bandgap ranging from 0.68 eV (x = 1) to 3.43 eV (x = 0), covering the full visible spectrum. This characteristic makes them suitable for visible light-emitting devices and for photovoltaic applications.[5,6] InGaN quantum well structures are currently used in light emitting diodes (LEDs)[2,56] and laser diodes.[3,57] These materials are also of interest for the fabrication of solar cells with high energy-conversion efficiency.[2] While LED and laser structures rely on thin InGaN quantum well layers, solar cells require thick InGaN films (thicker than 100 nm) in order to significantly absorb solar radiation.[58,59]

The growth of high quality GaN thin films by metal-organic chemical vapor deposition (MOCVD) requires growth temperatures above 1000°C, for efficient dissociation of NH_3.[1,60–63] The In-N bonds are thermally less stable than the Ga-N bonds, with cohesive energies of 1.93 and 2.24 eV/bond,[64] respectively, and tend to dissociate at the GaN growth temperatures. For that reason, InN is usually grown at temperatures below 900°C, at the expense of inefficient dissociation of NH_3.[65] At low temperatures, however, the equilibrium vapor pressures of liquid indium and InN are very similar, which leads to the coexistence of InN surfaces and indium droplets.[66] The requirement of high temperature to dissociate ammonia and low temperature for indium incorporation creates a narrow window for growth of high quality InGaN films. Furthermore, $In_xGa_{1-x}N$ films grown epitaxially on GaN have a large lattice mismatch (~ 1% for x = 0.1). The bi-axial misfit

* Parts of this chapter have been published as:
S. Wang, X. Hongen, H. Liu, A. M. Fischer, H. McFavilen, and F. A. Ponce, "Dislocation baskets in thick $In_xGa_{1-x}N$ epilayers," Submitted to J. Appl. Phys. on May 29, 2018.

strain along the basal-plane heterointerface does not provide a shear component for plastic relaxation along the primary $\{0001\}\langle 11\bar{2}0\rangle$ slip system.[67] For low indium content ($0 < x \leq 0.07$) the misfit strain is elastic in nature and the epitaxial films grow pseudomorphically on the GaN underlayer.[65] For indium content $x \geq 0.15$, the misfit strain is sufficient to trigger plastic relaxation via a punch-out mechanism involving slip on inclined prismatic planes.[68]

This chapter focuses on the structural and optical properties of $In_xGa_{1-x}N$ films with indium composition in the intermediate range between elastic deformation and full plastic relaxation ($0.07 \leq x \leq 0.12$). It has been observed that while the InGaN films tend to grow pseudomorphically strained, dislocation arrays resembling *baskets* are observed in this composition range. The presence of the dislocation baskets was unexpected, and we have performed in depth analysis of their properties. The findings indicate that the baskets enclose regions with higher indium content exhibiting luminescence at longer wavelengths, with *a*-type edge dislocations at their boundaries that relieve the lattice mismatch resulting from the change in indium content. I argue that the dislocation baskets originate from the simultaneous strain relaxation satisfying the crystal symmetry.

5.2 Experimental details

The InGaN films were grown by MOCVD at nominal temperatures of 790 and 760°C, on GaN layers grown on (0001) sapphire substrates, using a standard two-step process,[61] in a Veeco D180 reactor.[*] The InGaN films were grown to a thickness of 200 nm. The respective indium contents of x = 0.07 and 0.12, were measured by x-ray diffraction and

[*] The InGaN films were grown by Dr. Heather McFavilen at PhotoNitride Devices Inc., Tempe, Arizona

by Rutherford backscattering spectroscopy (RBS). Transmission electron microscopy (TEM) was used to study the microstructure of the epilayers. TEM samples were prepared by mechanical polishing and Ar^+ ion milling at 3.7 kV followed by 2.0 kV at liquid nitrogen temperatures. The TEM images were obtained in a FEI Titan 300/80 instrument operated at an accelerating voltage of 300 kV. Large-angle convergent-beam electron diffraction (LACBED) images were obtained in a JEOL 2010F instrument operated at 200 kV.[*] Energy dispersive X-ray (EDX) spectra were acquired in a JEOL ARM200F scanning TEM operated at 200 kV.

The optical properties were measured using cathodoluminescence (CL) in a scanning electron microscope with an acceleration voltage of 3 kV and a beam current of 500 pA, at 4.7K. Monochromatic CL images were obtained by setting the grating in the spectrometer for specific wavelengths and recording the spatial distribution of light emission. The light emission intensity was measured using a GaAs photomultiplier detector.[†]

5.3 Results and discussion

5.3.1 Microstructure of $In_xGa_{1-x}N$ films with x = 0.07

Figure 5.1 shows TEM images for an $In_xGa_{1-x}N$ film with $x = 0.07$. Each image shows a dislocation cluster, observed under two-beam diffraction-contrast conditions. The dislocation cluster in Figure 5.1(a) is viewed in cross section under dark-field conditions, and consists of an array of inclined dislocations originating at a base, resembling a *basket*. Figure 5.1(b) is a plan-view bright-field image, taken with the specimen tilted away from

[*] Parts of the TEM images and LACBED patterns were taken by Dr. Hongen Xie at Arizona State University.
[†] The cathodoluminescence measurements were performed by Dr. Alec Fischer and Mr. Hanxiao Liu at Arizona State University.

exact [0001] zone axis to produce a $\boldsymbol{g} = 11\bar{2}0$ diffraction condition. It reveals the arrangement of the inclined dislocations around the base. The dotted-line contrast along each dislocation reflects the relative inclination of the dislocation – this is due to electron beam interference between the sample surface and the dislocation. The basket is ~200 nm in diameter at the base, and contains 12 dislocations. The basket density was measured from large-area micrographs to be less than $1x10^7$ cm^{-2}.

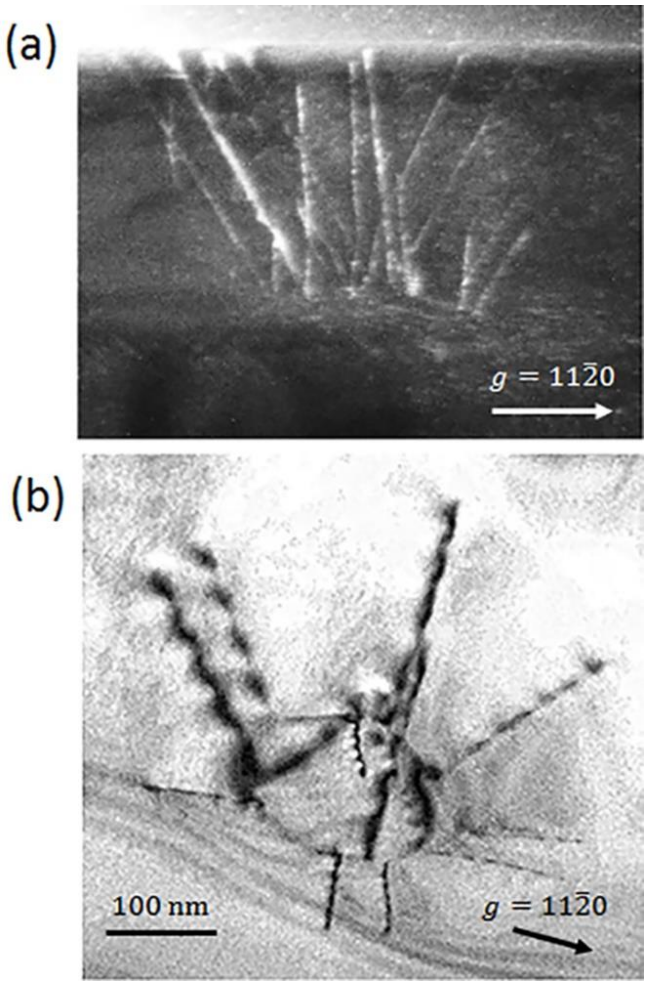

Figure 5.1. Dislocation clusters in an $In_xGa_{1-x}N$ film with x = 0.07, observed under two-beam diffraction-contrast TEM imaging conditions. (a) Dark field cross-section image under $\boldsymbol{g} = 11\bar{2}0$. (b) Bright field plan-view image under $\boldsymbol{g} = 11\bar{2}0$. The images correspond to different samples prepared specifically for cross-section and plan-view.

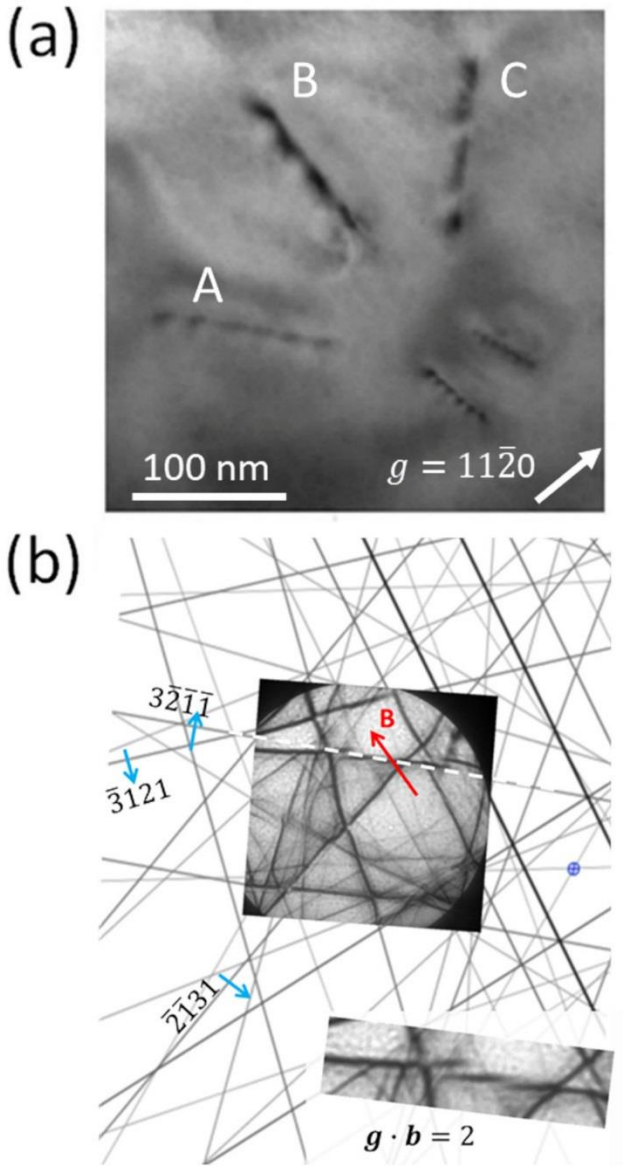

Figure 5.2. The Burgers vectors of the dislocations in a dislocation basket in the $In_{0.07}Ga_{0.93}N$ film were determined by LACBED. (a) The dislocations of a basket imaged under two-beam diffraction-contrast conditions. (b) LACBED pattern (center) above a simulation of Bragg lines near the $[10\bar{1}4]$ zone (background). The dislocation line B (red arrow) intersects the $3\bar{2}\bar{1}\bar{1}$ (equivalent to $3\bar{2}\bar{1}$) Bragg line (white dashed line), generating a split of $|\boldsymbol{g} \cdot \boldsymbol{b}| = 2$ (magnified below).

The Burgers vectors of the threading dislocations in the baskets was determined by LACBED.[69] In order to minimize interference from adjacent dislocations, a smaller basket

containing a few dislocations with the base removed was used for this determination. The characteristics of the dislocations in the basket are analyzed in Figure 5.2(a), which was taken in plan-view, with the sample tilted close to the $[10\bar{1}4]$ zone. An example of the LACBED analysis series is given in Figure 5.2(b).

Different Bragg lines were brought into the bright-field diffraction disk by tilting the incident electron beam. The dislocation line was brought to intersect a certain Bragg line by laterally shifting the sample while carefully keeping track of the position of the dislocation line. The Bragg line in Figure 5.2(b) (magnified in the bottom inset) intersecting a dislocation splits into fringes that depend on the Burgers vector of the dislocation and on the nature of the Bragg line. The magnitude of $\boldsymbol{g} \cdot \boldsymbol{b}$ is given by the number of subsidiary fringes in between the main Bragg line, according to the Cherns and Preston rules:[16]

$$|\boldsymbol{g} \cdot \boldsymbol{b}| = m + 1 \qquad (5.1)$$

where $\boldsymbol{g}$ is the reciprocal lattice vector associated with the Bragg line, $\boldsymbol{b}$ is the Burgers vector of the dislocation, *m* is the number of subsidiary fringes at the intersection. The sign of $\boldsymbol{g} \cdot \boldsymbol{b}$ is determined by the direction of the dislocation, the positive direction of the deviation parameter and the asymmetric splitting at the intersection.[16] The example in Figure 5.2(b) gives $\boldsymbol{g} \cdot \boldsymbol{b} = 2$. The simulation of Bragg lines near the $[10\bar{1}4]$ zone (background of Fig. 2(b)) was acquired in a JEMS software using the lattice parameters of GaN. The LACBED pattern was matched with the simulation to identify $\boldsymbol{g}$ of the Bragg line, which is $3\bar{2}\bar{1}\bar{1}$ in the example. These steps were carried out three times with different $\boldsymbol{g}$'s for a single dislocation, and thus the three components of the Burgers vector of the dislocation were determined. Table 5.1 lists the direction of each of the three dislocations,

the indices of each Bragg line, the values of $\boldsymbol{g} \cdot \boldsymbol{b}$ and Burgers vector of each dislocation. The dislocations are found to be of the pure edge type in all cases, with the Burger vector equal to one of the basal lattice vectors $\boldsymbol{a}$. Combining the Burgers vector and the line direction of the dislocation, the threading dislocations are found to correspond to the termination of missing $\{1\bar{1}00\}$ planes in the volume bounded by the baskets, which is schematically shown in Figure 5.3.

Table 5.1. Burgers vectors determined by LACBED and directions of dislocation lines.

	A			B			C		
g	$\bar{2}\,4\,0$	$4\,1\,\bar{2}$	$\bar{2}\,\bar{1}\,1$	$\bar{3}\,1\,1$	$\bar{2}\,\bar{1}\,1$	$3\,\bar{2}\,\bar{1}$	$\bar{2}\,4\,0$	$1\,\bar{3}\,0$	$3\,\bar{2}\,\bar{1}$
$g \cdot b$	-2	4	-2	-1	1	2	-2	2	-1
b	$[100] = 1/3[2\bar{1}\bar{1}0]$			$[0\bar{1}0] = 1/3[1\bar{2}10]$			$[\bar{1}\bar{1}0] = 1/3[\bar{1}\bar{1}20]$		
L	$[01\bar{1}0]$			$[10\bar{1}0]$			$[1\bar{1}00]$		

L is the direction of the projection of the dislocation line along the basal plane.
Note: In hexagonal symmetry, the three-index notation for a direction $[hkl]$ is equivalent to a four-index notation $[uvtw]$ through the following equations:
$u = \frac{1}{3}(2h - k),\ v = \frac{1}{3}(2k - h),\ t = -(u + v),\ w = l.$
The three-index notation for a plane (hkl) is equivalent to a four-index notation $(hkil)$, by adding a redundant index $i = -(h + k)$.

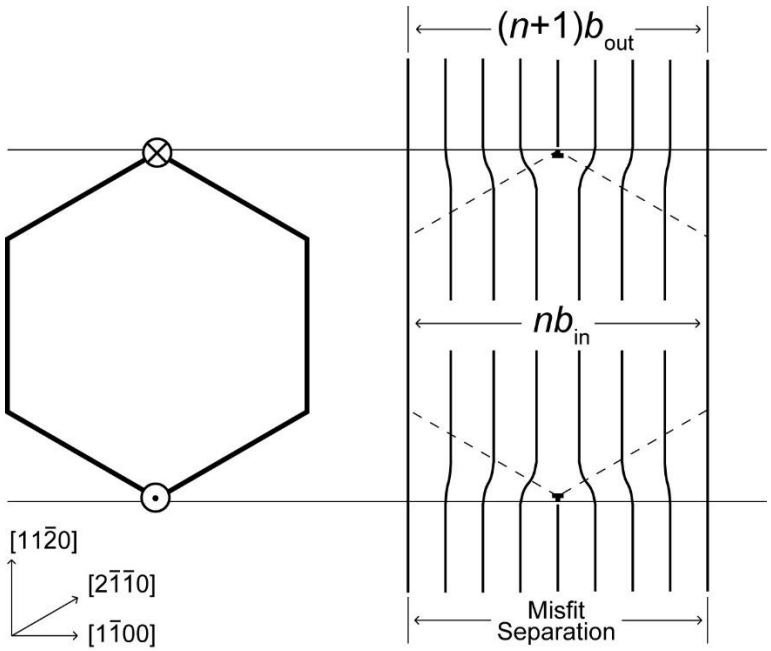

Figure 5.3. Schematic diagram of a cross section parallel to the basal plane above the base of the basket showing the missing $\{1\bar{1}00\}$ plane inside. Note the extra external planes associated with the threading edge dislocations. The lateral dimensions of the hexagon correspond to the vanishing of the misfit strain, which is equivalent to the separation of misfit dislocations in a periodic array.

5.3.2 Microstructure of $In_xGa_{1-x}N$ films with x = 0.12

Dislocation baskets are also observed in $In_xGa_{1-x}N$ films with $x = 0.12$. In the cross-section TEM image in Figure 5.4(a), it is observed that not all baskets start from the InGaN/GaN interface, with some of them being ~ 70 nm above the interface. The density of the baskets in this film is ~ $1x10^8$ cm^{-2}. From the plan-view image in Figure 5.4(b), the dislocation basket (on the right) is ~ 500 nm in diameter with ~ 20 dislocations.

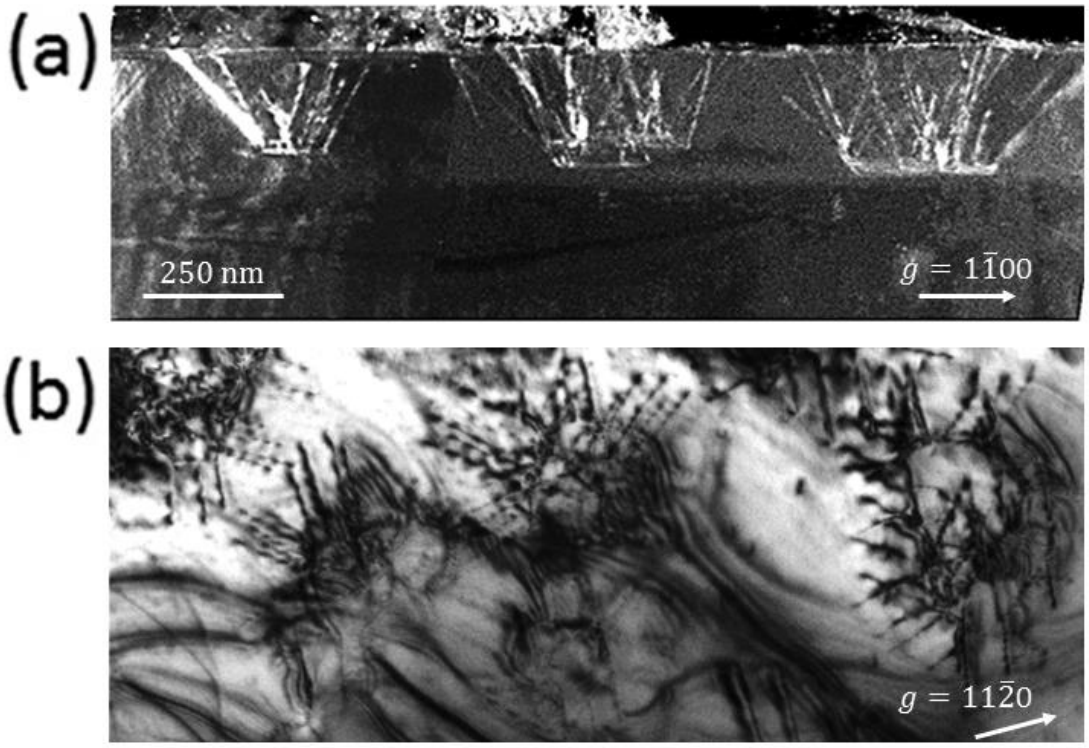

Figure 5.4. Dislocation clusters in an $In_xGa_{1-x}N$ film with x = 0.12, observed under two-beam diffraction-contrast TEM imaging conditions. (a) Dark field cross-section image under $\boldsymbol{g} = 1\bar{1}00$. (b) Bright field plan-view image under $\boldsymbol{g} = 11\bar{2}0$.

Discontinuities were not observed at the top surface between the matrix and baskets. No horizontal misfit dislocations were observed, which would be related to the difference in lattice parameter between basket and matrix. So, the lattice is elastically strained in the *c*-direction in order to resolve the difference in the *c*-lattice parameter.

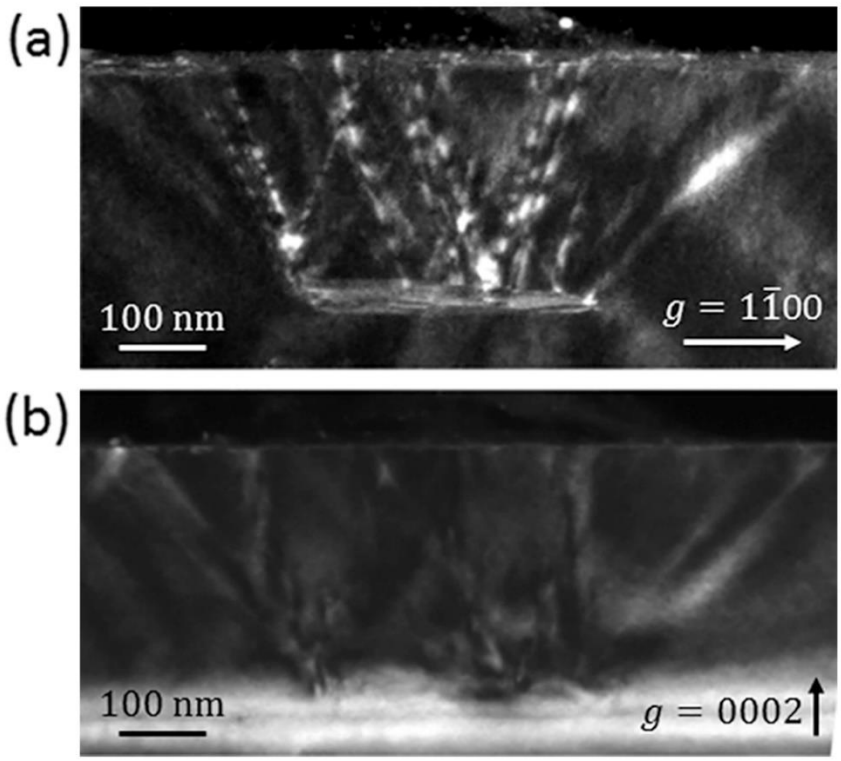

Figure 5.5. Cross-sectional TEM images of dislocation baskets in the $In_{0.12}Ga_{0.88}N$ film under (a) $\boldsymbol{g} = 1\bar{1}00$ and (b) $\boldsymbol{g} = 0002$.

Figure 5.5 shows the cross-section of dislocation baskets in the $In_{0.12}Ga_{0.88}N$ film. The fact that dislocations are visible under $\boldsymbol{g} = 11\bar{2}0$ (Figure 5.5(a)) but not under $\boldsymbol{g} = 0002$ (Figure 5.5(b)) confirms that the dislocation Burgers vectors are in the basal plane, having no component along the [0001] direction. Similarly, by comparing the plan-view images under $\boldsymbol{g} = 11\bar{2}0$ (Figure 5.6(a)) and $\boldsymbol{g} = 1\bar{1}00$ (Figure 5.6(b)), it's observed that dislocations along $[1\bar{1}00]$ disappear under $\boldsymbol{g} = 1\bar{1}00$. This indicates that the Burgers vectors are parallel to $[11\bar{2}0]$, perpendicular to $\boldsymbol{g} = 1\bar{1}00$. So, the Burgers vectors are found to be in the basal plane and along $\boldsymbol{a}$ directions, which is consistent with the LACBED study on the $In_{0.07}Ga_{0.93}N$ film.

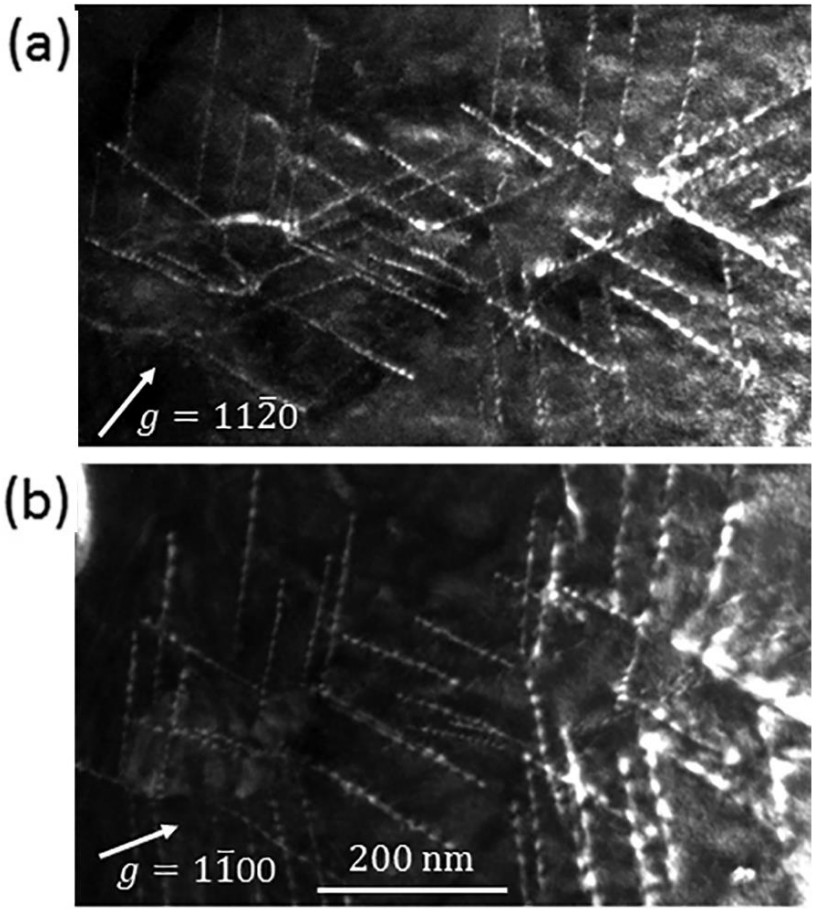

Figure 5.6. Plan-view TEM images of dislocation baskets in the $In_{0.12}Ga_{0.88}N$ film under (a) $\boldsymbol{g} = 11\bar{2}0$ and (b) $\boldsymbol{g} = 1\bar{1}00$ condition.

Next, I want to understand the nature of the base of the baskets. In Figure 5.7, the cross-section TEM specimen was tilted ~20° away from the basal plane in order to have an inclined view of the basket base. Under $\boldsymbol{g} = 11\bar{2}0$ in Figure 5.7(a), the base exhibits no evidence of misfit dislocations, which is consistent with the plan-view images in Figure 5.6. Under $\boldsymbol{g} = 1\bar{1}00$ in Figure 5.7(b), the base shows some fringes with the appearance of stacking faults. The difference between Figure 5.7(a) and (b) is due to the invisibility of stacking faults under $\boldsymbol{g} = 11\bar{2}0$, according to visibility criteria.[70]

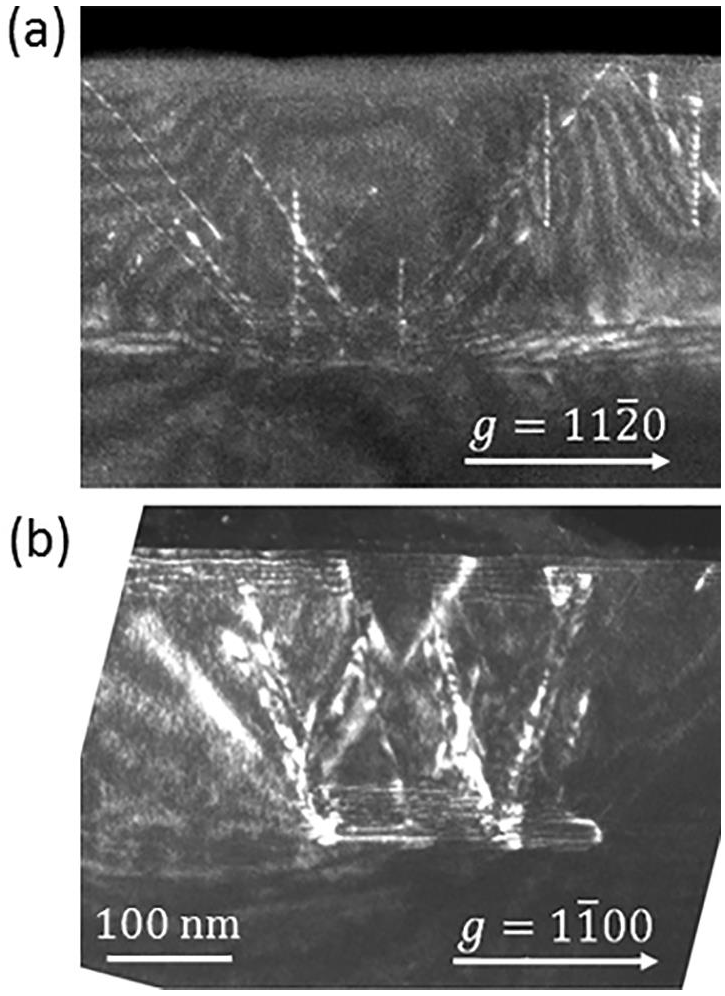

Figure 5.7. TEM images of the dislocation baskets in the $In_{0.12}Ga_{0.88}N$ film taken with the sample tilted away from edge-on direction by a large angle. (a) Image under $\boldsymbol{g} = 11\bar{2}0$ condition showing no misfit dislocations. (b) Image under $\boldsymbol{g} = 1\bar{1}00$ showing contrast like a stacking fault.

5.3.3 Optical properties of dislocation baskets

The optical properties of the baskets were studied using CL spectroscopy at 4.7 K. The spectrum in Figure 5.8(a) was taken from a surface area of ~ 25 um^2 of the $In_xGa_{1-x}N$ film with x = 0.07. The emission peak is clearly asymmetric, and can be fitted by two Gaussian peaks. Figure 5.8(b) shows two spot-mode spectra, one taken from inside the basket and the other from the surrounding matrix. The probe size in spot mode is ~100 nm^2,

which is sufficiently small to be confined in the basket region. The surrounding InGaN film exhibits a peak at 3.15 eV, while the peak from the basket is red-shifted to 3.12 eV, indicating a higher indium content. Monochromatic CL images were taken at the energy of the two peaks. Figure 5.8(c) corresponds to the peak of the baskets, at 3.12 eV. The density of the bright spots in this area is ~ 1 x 10^8 cm^{-2}, which is higher than the density of baskets observed in TEM images. This discrepancy will be discussed later. Figure 5.8(d), taken at 3.15 eV, shows complementary contrast as Figure 5.8(c). The two monochromatic images confirm that the CL emission in Figure 5.8(a) is the sum of peaks from the baskets and the matrix.

The CL emission is correlated with the bandgap energy (E_g) of $In_xGa_{1-x}N$, which is given by

$$E_{g,\mathrm{InGaN}}(x) = xE_{g,\mathrm{InN}} + (1-x)E_{g,\mathrm{GaN}} - b \cdot x(1-x) \qquad (5.2)$$

using $E_{g,\mathrm{InN}} = 0.675$ eV at low temperature, and a bowing parameter $b = 1.65$.[53] It is found that the indium content in the baskets (emitting at 3.12 eV) is $x \approx 0.09$ and the rest of the film (emitting at 3.15 eV) has an indium content $x \approx 0.07$. The presence of more indium in the baskets is attributed to the misfit strain relaxation in the baskets by the threading edge dislocations on the boundary of the baskets that open up the lattice for the incorporation of additional indium content.

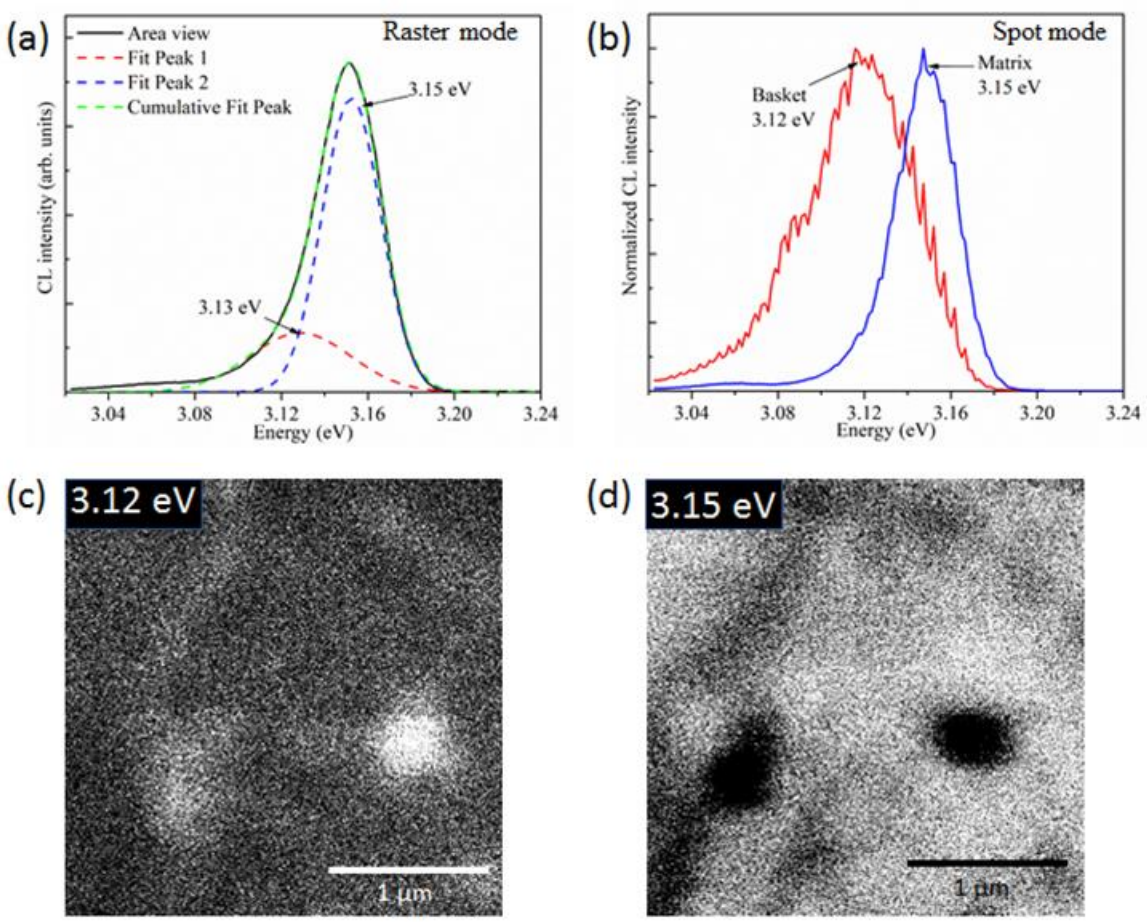

Figure 5.8. (a) Full CL spectrum of the $In_{0.07}Ga_{0.93}N$ thin film. The dashed lines are from Gaussian peak fitting. (b) Spot mode spectra at a basket (red, peak at 3.12 eV) and the matrix (blue, peak at 3.15 eV). Monochromatic images at (c) 3.12 eV and (d) 3.15 eV.

Similar analysis was performed on the $In_{0.12}Ga_{0.88}N$ film, shown in Figure 5.9. The two peaks at 2.93 eV and 2.99 eV indicate the indium content to be $x \approx 0.14$ in the baskets, and $x \approx 0.12$ in the matrix. The CL images in Figure 5.9(c) and (d) also exhibit a complementary contrast like for the $In_{0.07}Ga_{0.93}N$ film, but with a higher density of baskets.

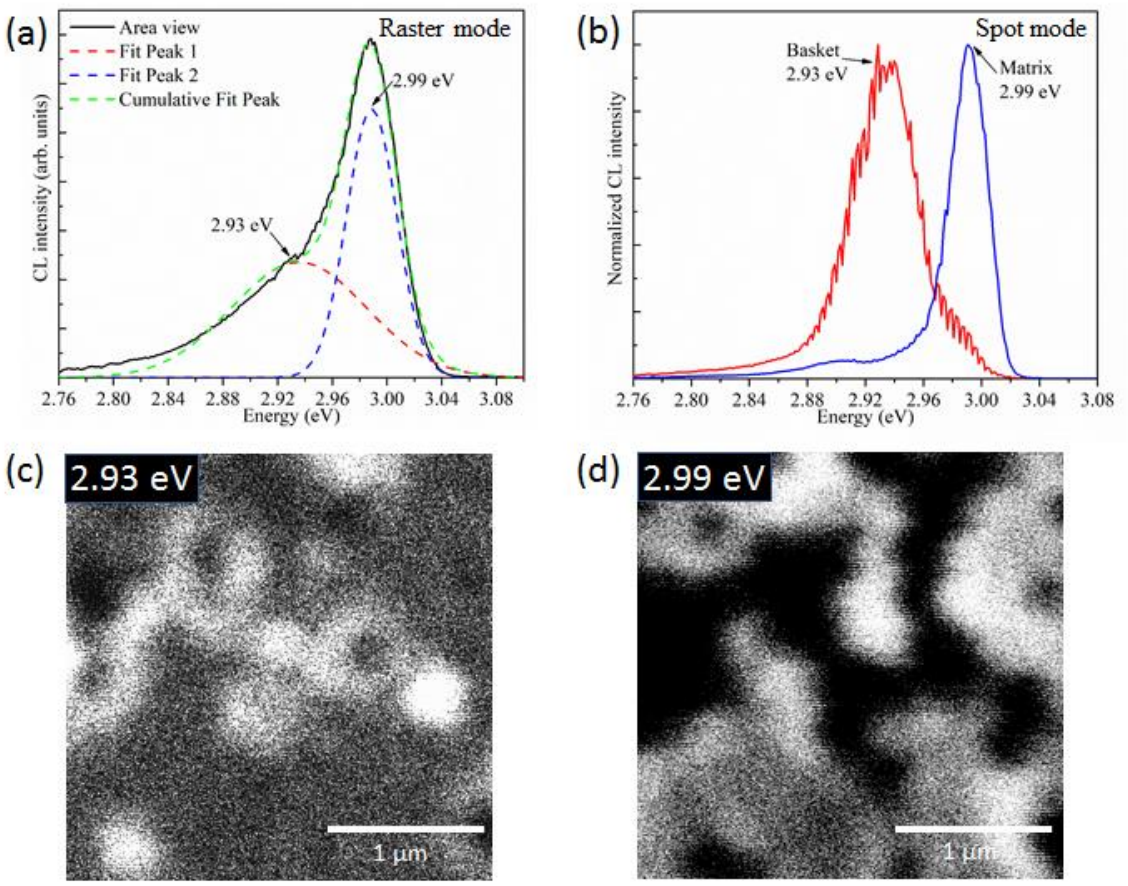

Figure 5.9. (a) Full CL spectrum of the $In_{0.12}Ga_{0.88}N$ thin film. The dashed lines are from Gaussian peak fitting. (b) Spot mode spectra at a basket (red, peak at 2.93 eV) and the matrix (blue, peak at 2.99 eV). Monochromatic images at (c) 2.93 eV and (d) 2.99 eV.

The excess density of bright spots in the CL images can be attributed to the existence of pyramidal pits, as observed in Figure 5.10. The pits are generated from screw-component threading dislocation cores that open up during growth of the InGaN epilayer. Elastic relaxation occurs around the pits, allowing incorporation of higher indium content, and exhibiting CL emission at longer wavelengths.[65] With similar relaxation mechanisms, the pyramidal pits should have the same indium content as the baskets, so they are not distinguishable from the baskets in the monochromatic CL images. The density of the pits

is determined from TEM analysis to be in the middle 10^8 cm^{-2} for both x = 0.07 and 0.12 $In_xGa_{1-x}N$ films. In Figure 5.8(c), most of the bright spots should be the pyramidal pits for the $In_{0.07}Ga_{0.93}N$ film. In Figure 5.9(c), the higher density of the bright spots is related to the higher density of baskets in the $In_{0.12}Ga_{0.88}N$ film, where both the pits and the baskets are at the 10^8 cm^{-2} order of magnitude.

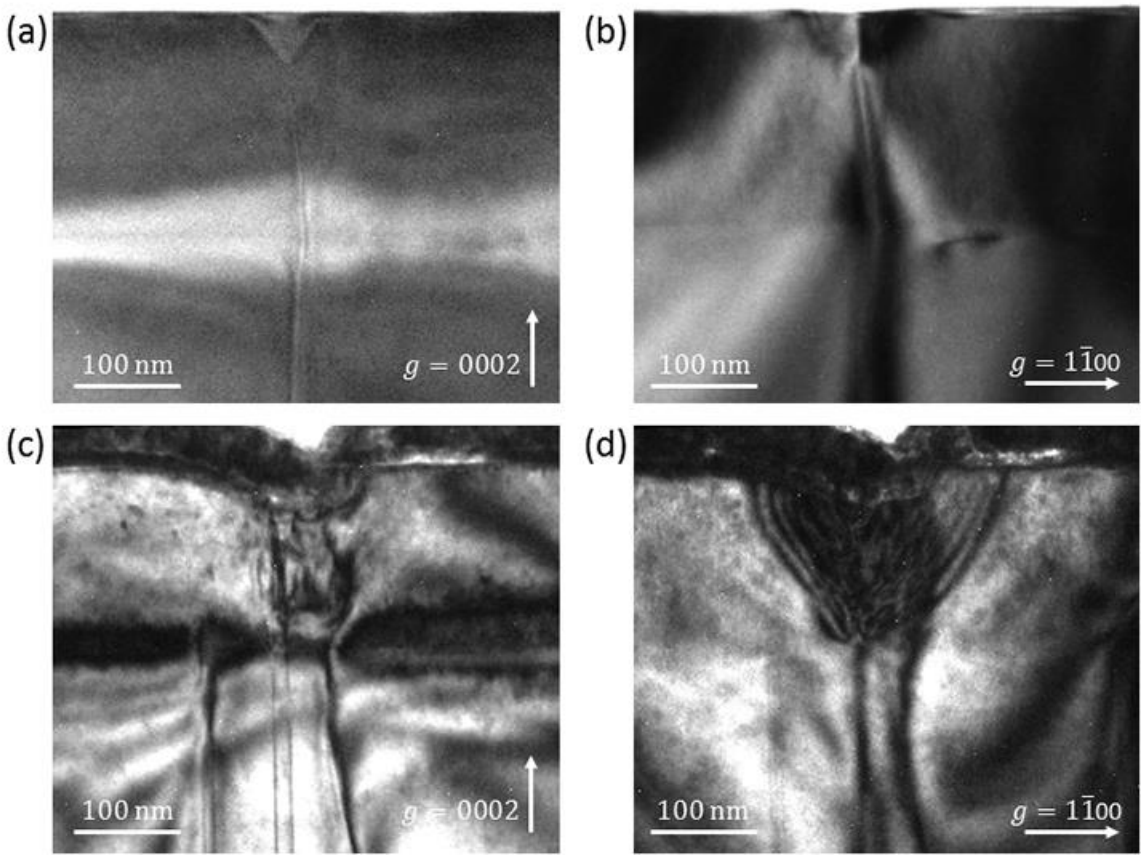

Figure 5.10. Two-beam bright field cross-sectional TEM images of pyramidal pits in $In_xGa_{1-x}N$ films with (a) and (b) x = 0.07, (c) and (d) x = 0.12.

5.3.4 EDX study of indium distribution

Variations in chemical composition can be measured using EDX. EDX mapping of the indium *L*-edge signal was acquired from the basket region in Figure 5.11(a). The solid

line in Figure 5.11(b) represents the vertical line scan of indium signal, from the top of the basket down to the GaN underlayer. The dashed line in Figure 5.11(b) is a reference vertical scan taken outside the basket. Each scan is consisted of 100 points, with a step size of about 2.5 Å, and a dwell time of 1.0s for each point. Below the basket base, the two scans coincide on the same amount of indium. Above the basket base, the scan shows a gradual increase in indium content, compared to the reference scan.

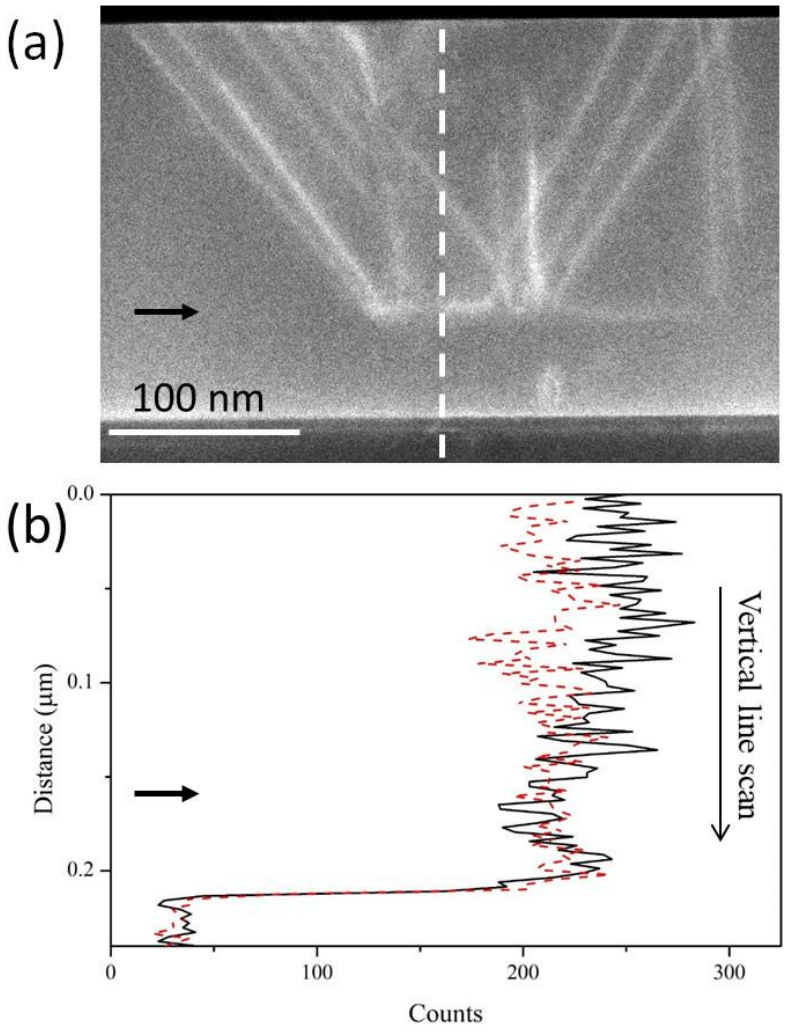

Figure 5.11. (a) HAADF image showing a basket in the $In_{0.12}Ga_{0.88}N$ sample. The white dashed line marks the position of the line scan. (b) EDX line scan of the indium *L*-peak

across the basket (black solid line). The basket base is indicated by the horizontal arrows. The red dashed line represents a reference scan outside the basket. An 18% increase in the indium signal is observed inside the basket.

The absolute value of indium content could not be obtained, due to lack of standard for the Cliff-Lorimer factors. An estimate of the indium content can be obtained from the difference of indium signal between inside and outside of the basket. The signal from the GaN underlayer (lowest portion of the scan) has a background indium signal, most likely from fluorescence from the indium atoms in the InGaN film that absorb X-rays from gallium atoms, which depends on the geometry of the TEM column and the position of EDX detector. After subtraction of background, the top part of the basket exhibits an ~18% increase of indium content, compared to outside the basket. This equals to an indium content of $x \approx 0.14$ in this region, assuming the matrix to be $x = 0.12$. This result closely follows the CL spectra discussed previously.

5.3.5 Strain relaxation inside the baskets

A missing plane inside a basket should be related to two threading edge dislocations at the boundary of the basket. This pair of dislocations should be part of a misfit dislocation loop, enabling strain relaxation inside the basket. The amount of strain relaxed by a periodic array of misfit edge dislocations is:

$$\delta = \frac{b_{\perp}}{d} \qquad (5.3)$$

where δ is the relative change of lattice parameter, $b_{\perp}$ is the edge component of the Burgers vector, and d is the period of spacing between dislocations.

I argue that in these samples the diameter of the basket base should be equal to the spacing between misfit dislocations. As illustrated in Figure 5.3, the misfit dislocation

separation represents the periodicity of the strain field on the basal plane, and at equilibrium the basket base rim lies where the strain is zero. Furthermore, when a basket contains *n* pairs of dislocations along each $[11\bar{2}0]$ direction, its diameter should be *n* times of the misfit dislocation separation. This relationship is observed experimentally and is summarized in Table 5.2. For a basket with 6 threading dislocations (two threading dislocations for each $\langle 11\bar{2}0 \rangle$ direction), the diameter is ~ 100 nm in both $In_xGa_{1-x}N$ films with $x = 0.07$ and 0.12. This is equivalent to a misfit dislocation separation of ~ 100 nm. For the ~ 2% increase in indium composition observed by CL and EDX, the calculated separation would be 124.7 and 126.2 nm for $x = 0.07$ and $x = 0.12$, respectively, consistent with the experimental observations.

Table 5.2. Summary of basket base diameters vs. number of dislocations for $In_xGa_{1-x}N$.

$x = 0.07$			$x = 0.12$		
In Figure	Diameter (nm)	Number of dislocations	In Figure	Diameter (nm)	Number of dislocations
Figure 5.1a	200	14	Figure 5.4a, left basket	120	8
Figure 5.1b	200	12	Figure 5.4a, middle basket	250	18
Figure 5.2a	100	6	Figure 5.4a, right basket	220	16

5.3.6 Formation of baskets

The presence of similar dislocation clusters has been previously reported by Meng et al.,[71] which covered a similar range of indium concentrations. They reported that the base of the baskets consists of stacking faults, and that the Shockley partials on the stacking

fault peripheries can dissociate to generate ***a***-type threading dislocations. Here I report the observation of some baskets where the base does not exhibit lattice translations such as due to stacking faults. Such characteristics are attributed to simultaneous relaxation following the crystal symmetry, where the simultaneous dissociation of misfit dislocations along three equivalent directions result in stacking fault translations whose vector sum is zero. Detailed explanations are provided in the following:

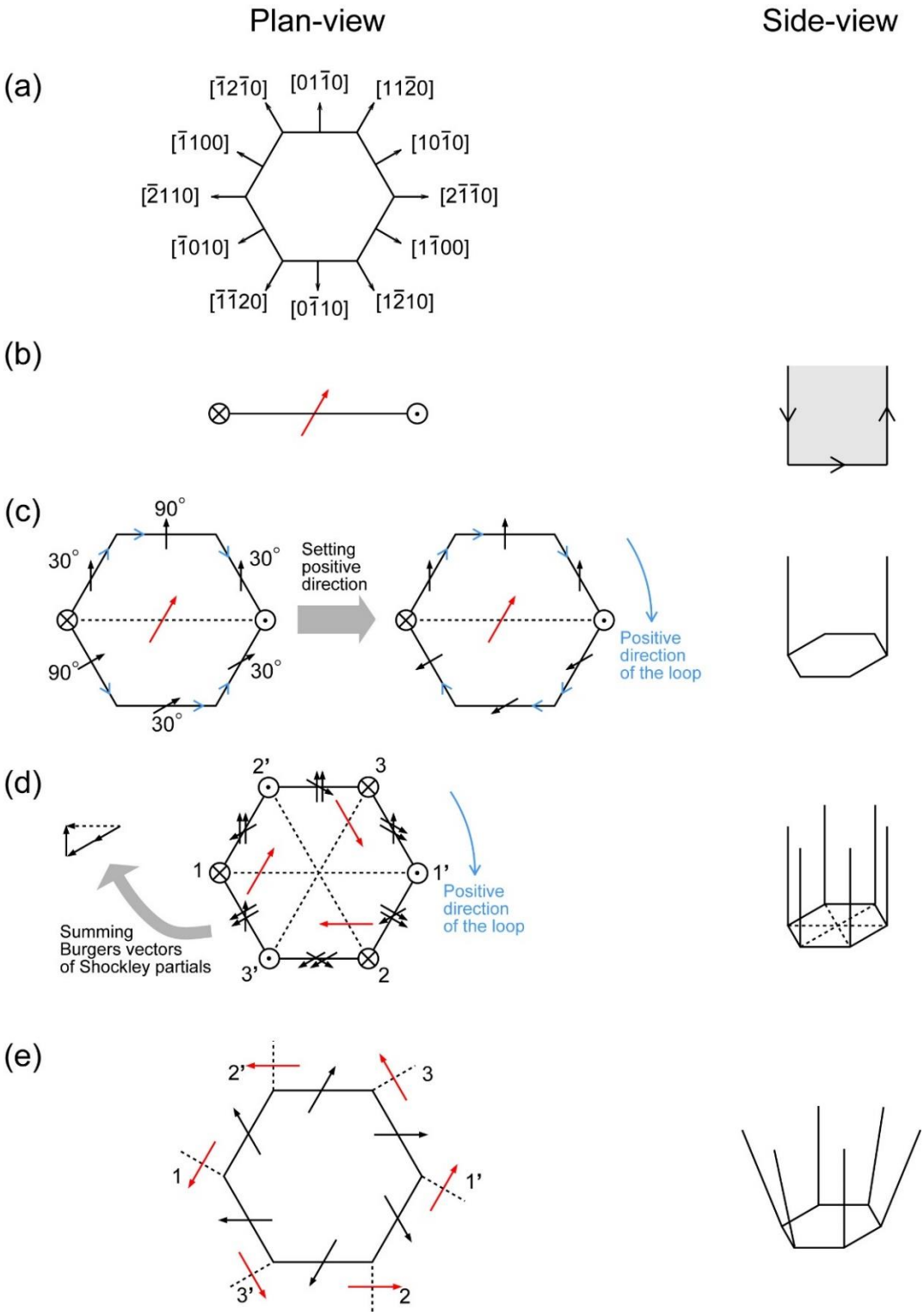

Figure 5.12. Schematic drawings of the plan-views and side-views of the interaction between misfit dislocations and stacking faults. (a) Indexing of directions on the basal

plane. (b) A dislocation half-loop. The segment on the basal plane is a 60°-dislocation, with Burgers vector $\boldsymbol{b} = \frac{1}{3}[11\bar{2}0]$ as indicated by the red arrow. The circles at the two ends denote the two segments in c- and $\bar{c}$-directions. (c) The 60°-dislocation expanding into a stacking fault surrounded by 30°- and 90°-Shockley partials, whose Burgers vectors are indicated by the black arrows. The line directions of the Shockley partials are indicated by the blue arrows. After choosing clockwise as the positive direction of the Shockley partial loop, the line directions and Burgers vectors in the bottom half need to be reversed. The displacement vector of the stacking fault is $\boldsymbol{R} = \frac{1}{3}[10\bar{1}0]$. (d) Overlapping of three misfit half-loops in different orientations 120° away from each other. The numbers 1-3 mark the three pairs of threading dislocations. (e) The final arrangement of the dislocations. The threading dislocations are inclined to the $\langle 1\bar{1}00\rangle$ directions.

To facilitate the discussion, the various directions on the basal plane are shown in Figure 5.12(a). A misfit dislocation half-loop can be generated to relax the strain in the InGaN film, with a missing plane inside the half-loop, as shown in Figure 5.12(b). The segment on the basal plane is a 60°-dislocation, say the dislocation line along $\boldsymbol{L} = \frac{1}{3}[\bar{1}2\bar{1}0]$, and the Burgers vector $\boldsymbol{b} = \frac{1}{3}[\bar{2}110]$. The edge-type threading segments are in the $\pm c$-directions, with the same Burgers vector as the basal segment. The 60°-dislocation can dissociate into 30°- and 90°-Shockley partials,[72] as shown in Figure 5.12(c). The Burgers vectors are $\frac{1}{3}[10\bar{1}0]$ for the bottom half and $\frac{1}{3}[01\bar{1}0]$ for the top half of the Shockley partial loop. The loop surrounds a stacking fault, with a displacement vector $\boldsymbol{R} = \frac{1}{3}[10\bar{1}0]$. Note that in Figure 5.12(c) the bottom portion of the loop corresponds to the displacement of the 30° partial parallel to the original 60° full dislocation. The hexagonal shape of the loop results in the lower left portion being a 90° partial and the lower right portion being a 30° partial. A similar situation is with the top portion of the loop corresponding to a 90° partial parallel to the original 60° full dislocation, with the left and right upper portions being 30° partials.

The dissociation width between the two partials is determined by two factors: (1) the repulsive interaction between the partial-dislocation strain fields, and (2) the energy required to generate a stacking fault, which is proportional to its area.[73] In this model, the dissociation width should be the same as the distance between misfit dislocations, considering the periodicity of the strain field on the basal plane. The strain relaxation contributed by this effect has been discussed in Section 5.3.5.

Before moving to the next step, the dislocation line directions of the Shockley partials need to be revised. Initially in Figure 5.12(c), the partial dislocation lines are pointing to the right, following the trend of the original dislocation half-loop shown in Figure 5.12(b). Then, take the operation of setting all the line directions to be clockwise along the perimeter of the hexagon, as indicated by the blue arrows. This operation reserves the line directions, as well as the Burgers vectors of the Shockley partials in the bottom half. It is reasonable to do so, because the line direction and the Burgers vector direction of a dislocation are defined relative to each other. This operation will later allow us to add up the Burgers vectors.

Considering the symmetry of the wurtzite structure, misfit dislocations may simultaneously be generated along the three $\langle 11\bar{2}0\rangle$ directions in order to symmetrically relax the misfit strain. Figure 5.12(d) shows three misfit half-loops with Burgers vectors $\boldsymbol{b_1} = \frac{1}{3}[11\bar{2}0]$, $\boldsymbol{b_2} = \frac{1}{3}[\bar{2}110]$, and $\boldsymbol{b_3} = \frac{1}{3}[1\bar{2}10]$, following the three-fold symmetry of the basal plane. When the 60^o-dislocations dissociate and overlap on a single basal-plane stacking fault, the following can take place:

(1) Each side of the hexagon will be the result of the overlap of three Shockley partials. The sum of the three Burgers vectors will be $\frac{1}{3}\langle 11\bar{2}0\rangle$, equivalent to a 60° dislocation on each side, as shown in Figure 5.12(e), and in the following equations for the various sides of the hexagon:

$$
\begin{aligned}
&1 \rightarrow 2\text{'}: 2\times\tfrac{1}{3}[01\bar{1}0]+\tfrac{1}{3}[\bar{1}010]=\tfrac{1}{3}[\bar{1}2\bar{1}0]\\
&2\text{'} \rightarrow 3: 2\times\tfrac{1}{3}[01\bar{1}0]+\tfrac{1}{3}[1\bar{1}00]=\tfrac{1}{3}[11\bar{2}0]\\
&3 \rightarrow 1\text{'}: 2\times\tfrac{1}{3}[1\bar{1}00]+\tfrac{1}{3}[01\bar{1}0]=\tfrac{1}{3}[2\bar{1}\bar{1}0]\\
&1\text{'} \rightarrow 2: 2\times\tfrac{1}{3}[1\bar{1}00]+\tfrac{1}{3}[\bar{1}010]=\tfrac{1}{3}[1\bar{2}10]\\
&2 \rightarrow 3\text{'}: 2\times\tfrac{1}{3}[\bar{1}010]+\tfrac{1}{3}[1\bar{1}00]=\tfrac{1}{3}[\bar{1}\bar{1}20]\\
&3\text{'} \rightarrow 1: 2\times\tfrac{1}{3}[\bar{1}010]+\tfrac{1}{3}[01\bar{1}0]=\tfrac{1}{3}[\bar{2}110]
\end{aligned}
\qquad (5.4)
$$

These dislocations have the similar visibility as the threading dislocations, and can be seen in Figure 5.1(b). They are not visible in some plan-view images, such as Figure 5.2(a) and Figure 5.6, probably because the basket bases have been removed during sample preparation.

(2) The net displacement of the stacking fault will be $\boldsymbol{R_{sum}} = \frac{1}{3}[10\bar{1}0]+\frac{1}{3}[\bar{1}100]+\frac{1}{3}[0\bar{1}10]=0$, for a simultaneous symmetric relaxation. This is equivalent to no stacking fault at the base, which should happen when the perimeter consists of full dislocations. It's also possible that in some cases the relaxation is not entirely symmetric, resulting in a net stacking fault displacement along a $\langle 1\bar{1}00\rangle$ direction, as observed in Figure 5.7. For

example, the overlap of only two stacking faults gives $\boldsymbol{R_{sum}} = \frac{1}{3}[10\bar{1}0] + \frac{1}{3}[0\bar{1}10] = \frac{1}{3}[1\bar{1}00]$, which is still a stacking fault.

The threading dislocations are observed to incline towards $\langle 1\bar{1}00 \rangle$ directions, which has been reported to provide a biaxial strain relaxation[74]

$$\delta_{\text{avg}} = bL\rho/4 \qquad (5.5)$$

where ρ, L, and b are the density, the projected length onto the *c*-plane, and the Burgers vector of the dislocations. For example, the threading dislocation pair No. 1 and 1' in Figure 5.12(e) have their basal plane projection along the $[1\bar{1}00]$ direction, perpendicular to their Burgers vector $\frac{1}{3}[11\bar{2}0]$. This is consistent with the TEM observations in Figure 5.6. For a uniform convention where all threading dislocations are pointing in +*c*-direction, the Burgers vector of 1 (the left segment of the pair) is reversed, as reversing its dislocation line direction, following the same argument in Figure 5.12(c). Since the model is dealing with dislocation loop, which dissociate at the base, threading dislocations should occur in pairs. However, sometimes odd number of threading dislocations are observed emanating from the base of the basket. This can result from invisibility of an out-of-diffraction-contrast dislocation, or from a dislocation being too close to the projections of the image, or from the addition to a pre-existing threading dislocation.

The assumption that the basal plane dislocation that dissociates is a 60° dislocation can be justified as follows. Take the pair No. 1 and 1' as an example: If they are viewed along the $[\bar{2}110]$ direction, they should seem to originate from the same position on the base, and to incline towards opposite directions, forming a "V" shape — This is observed in Figure 5.6(b). And if they are viewed along the $[1\bar{1}00]$ direction, they should appear as

two c-direction lines separated by a distance — The two "vertical" lines in Figure 5.6(a) are the example. On the other hand, the assumption of a 90° dislocation will result in the opposite observations: the pair of dislocations will separate when viewed along the $[\bar{2}110]$ direction, and overlap when viewed along the $[1\bar{1}00]$ direction – This is contrary to the observations.

Thus, I have established a primary basket model consisting of three pairs of threading dislocations and a loop of 30°-Shockley partials, as shown in Figure 5.12(e). At each node of the hexagon, the two basal-plane dislocations will combine into a threading dislocation, following these equations:

$$\begin{aligned}
&1: \tfrac{1}{3}[\bar{2}110] + \tfrac{1}{3}[1\bar{2}10] = \tfrac{1}{3}[\bar{1}\bar{1}20] \\
&1': \tfrac{1}{3}[2\bar{1}\bar{1}0] + \tfrac{1}{3}[\bar{1}2\bar{1}0] = \tfrac{1}{3}[11\bar{2}0] \\
&2: \tfrac{1}{3}[1\bar{2}10] + \tfrac{1}{3}[11\bar{2}0] = \tfrac{1}{3}[2\bar{1}\bar{1}0] \\
&2': \tfrac{1}{3}[\bar{1}2\bar{1}0] + \tfrac{1}{3}[\bar{1}\bar{1}20] = \tfrac{1}{3}[\bar{2}110] \\
&3: \tfrac{1}{3}[11\bar{2}0] + \tfrac{1}{3}[\bar{2}110] = \tfrac{1}{3}[\bar{1}2\bar{1}0] \\
&3': \tfrac{1}{3}[\bar{1}\bar{1}20] + \tfrac{1}{3}[2\bar{1}\bar{1}0] = \tfrac{1}{3}[1\bar{2}10]
\end{aligned} \qquad (5.6)$$

Please note that in each equation, the Burgers vector of the latter basal-plane dislocation is reversed, in order to have the line directions of both basal-plane dislocations pointing towards the node.

For the baskets with many dislocations, as in the $In_{0.12}Ga_{0.88}N$ film, several primary baskets may be stacked along the *c*-direction, sharing the same base. The relaxation of strain would allow higher indium content to grow inside the baskets.

5.4 Conclusions

Dislocation arrays in the form of baskets have been observed in the $In_xGa_{1-x}N$ films with x = 0.07 and 0.12, with the density of the baskets increasing with indium content in the film. The nature of the dislocations in the baskets was studied using TEM diffraction techniques. These dislocations are found to be *a*-type edge dislocations, which accommodates the lattice mismatch of ~ 0.64% at the lateral boundaries of the baskets. This lattice mismatch is found due to increasing amount of indium inside the dislocation baskets which is revealed by the redshift of the bandgap luminescence by ~0.06 eV. The presence of lower bandgap regions associated with dislocation baskets leads to formation of traps for electrons and holes but the dislocations in the baskets do not act as non-radiative recombination centers. EDX mapping confirms the higher indium content in the baskets. I propose that the dislocation baskets are generated from misfit dislocation half loops. The basal plane segments of the half loops dissociate into Shockley partials and overlap to form the base of the baskets. The threading segments of the half loops incline to form the side walls of the baskets. It would be interesting to see if this symmetrical relaxation mechanism can be coherently extended throughout the plane of the film.

Chapter 6 Summary and Future Work

In summary, the structural properties of two groups of III-nitride semiconductors were studied by TEM and other techniques.

The BAlN thin films intended for DUV applications were discussed in Chapters 3 and 4. As the B/III gas-flow ratio increased from 0.06 to 0.18, the films maintained a wurtzite structure, while the microstructures showed trends towards finer tilted columns and twin formations. A discrepancy between the B content measured by XRD and RBS was observed, and was attributed to the B segregation at the columnar grain boundaries and twin boundaries. B interstitials, as well as other point defects are observed by low-loss EELS, and identified with the help of DFT calculations. These point defects were correlated to the microstructures of the films.

Future work on BAlN thin films may include the study of incorporation of boron in distributed Bragg reflector (DBR) structures. BAlN/AlN DBR can exhibit high reflectivity at DUV region, due to the high refractive index contrast and large bandgap.[8] The performance of the DBRs is affected by the structural properties and crystalline qualities.[8,11] Study of the structural properties of the BAlN material in a BAlN/AlN superlattice would be important for the realization of the DBRs. Another direction of future work may focus on the quantitative analysis of the point defects in BAlN films. The defect peaks shown in the AlN templates result solely from the delocalization of the point defects in the BAlN films. The densities of the peaks decrease with the distance to the BAlN/AlN interface. By carefully plotting this trend and modeling the delocalization effect in a

functional form, we may be able to acquire the density of the point defects, or locate single defect in a less defective film.

The thick InGaN films for a double-junction solar cell application were discussed in Chapter 5. Dislocation arrays resembling baskets were observed for indium compositions in the range $0.07 < x < 0.12$. The sides of baskets consist of threading dislocations of pure ***a***-type, while the bottom of baskets exhibited no misfit dislocations, and often no displacement from stacking faults. The inside of the baskets has a higher indium compositions, as observed by CL and EDX. The baskets could be generated from simultaneous and symmetric dissociation of misfit dislocation half loops, which allowed strain relaxation and higher indium content inside the baskets.

Future work on the InGaN films should focus on their electronic properties and carrier life times. Accelerated life time testing is usually performed at high temperatures. Understanding the changes in structural and optical properties during the annealing process would be important to the study of the failure process of InGaN materials, especially for high temperatures applications in concentrator photovoltaics.

REFERENCES

[1] H. Amano, M. Kito, K. Hiramatsu, and I. Akasaki, Jpn. J. Appl. Phys. **28**, L2112 (1989).

[2] S. Nakamura, M. Senoh, N. Iwasa, and S. Nagahama, Jpn. J. Appl. Phys. **34**, L797 (1995).

[3] S. Nakamura, M. Senoh, S. Nagahama, N. Iwasa, T. Yamada, T. Matsushita, H. Kiyoku, and Y. Sugimoto, Jpn. J. Appl. Phys. **35**, L74 (1996).

[4] I. Akasaki, S. Sota, H. Sakai, T. Tanaka, M. Koike, and H. Amano, Electron. Lett. **32**, 1105 (1996).

[5] J. Wu, W. Walukiewicz, K. M. Yu, W. Shan, J. W. Ager, E. E. Haller, H. Lu, W. J. Schaff, W. K. Metzger, and S. Kurtz, J. Appl. Phys. **94**, 6477 (2003).

[6] F. A. Ponce and D. P. Bour, Nature **386**, 351 (1997).

[7] M. Zhang and X. Li, Phys. Status Solidi B **254**, 1600749 (2017).

[8] M. Abid, T. Moudakir, G. Orsal, S. Gautier, A. En Naciri, Z. Djebbour, J.-H. Ryou, G. Patriarche, L. Largeau, H. J. Kim, Z. Lochner, K. Pantzas, D. Alamarguy, F. Jomard, R. D. Dupuis, J.-P. Salvestrini, P. L. Voss, and A. Ougazzaden, Appl. Phys. Lett. **100**, 051101 (2012).

[9] C. H. Wei and J. H. Edgar, J. Cryst. Growth **208**, 179 (2000).

[10] X. Li, S. Sundaram, Y. El Gmili, T. Moudakir, F. Genty, S. Bouchoule, G. Patriarche, R. D. Dupuis, P. L. Voss, J. P. Salvestrini, and A. Ougazzaden, Phys. Status Solidi A **212**, 745 (2015).

[11] X. Li, S. Sundaram, Y. El Gmili, F. Genty, S. Bouchoule, G. Patriache, P. Disseix, F. Réveret, J. Leymarie, J.-P. Salvestrini, R. D. Dupuis, P. L. Voss, and A. Ougazzaden, J. Cryst. Growth **414**, 119 (2015).

[12] A. G. Bhuiyan, K. Sugita, A. Hashimoto, and A. Yamamoto, IEEE J. Photovoltaics **2**, 276 (2012).

[13] W. Shockley and H. J. Queisser, J. Appl. Phys. **32**, 510 (1961).

[14] D. B. Williams and C. B. Carter, *Transmission Electron Microscopy: A Textbook for Materials Science*, 2nd ed. (Springer, New York, 2009), pp. 7, 153, 379, 680.

[15] J. P. Morniroli, *Large-Angle Convergent-Beam Electron Diffraction (LACBED): Applications to Crystal Defects* (French Society of Microscopies, Paris, 2002), p. 3.

[16] D. Cherns and A. R. Preston, J. Electron Microsc. Tech. **13**, 111 (1989).

[17] J. P. Morniroli, J. Microsc. **223**, 240 (2006).

[18] A. Howie and M. J. Whelan, Proc. R. Soc. A Math. Phys. Eng. Sci. **263**, 217 (1961).

[19] M. Vulović, L. M. Voortman, L. J. van Vliet, and B. Rieger, Ultramicroscopy **136**, 61 (2014).

[20] M. J. Whelan and P. B. Hirsch, Philos. Mag. **2**, 1121 (1957).

[21] S. J. Pennycook and D. E. Jesson, Ultramicroscopy **37**, 14 (1991).

[22] J. I. Langford and A. J. C. Wilson, J. Appl. Crystallogr. **11**, 102 (1978).

[23] E. Zolotoyabko, *Basic Concepts of X-Ray Diffraction* (Wiley-VCH, Weinheim, 2014), p. 141.

[24] J. Perrière, Vacuum **37**, 429 (1987).

[25] P. Hohenberg and W. Kohn, Phys. Rev. **136**, B864 (1964).

[26] W. Kohn and L. J. Sham, Phys. Rev. **140**, A1133 (1965).

[27] A. Ougazzaden, S. Gautier, C. Sartel, N. Maloufi, J. Martin, and F. Jomard, J. Cryst. Growth **298**, 316 (2007).

[28] T. Akasaka, Y. Kobayashi, and T. Makimoto, J. Cryst. Growth **298**, 320 (2007).

[29] V. Ravindran, M. Boucherit, A. Soltani, S. Gautier, T. Moudakir, J. Dickerson, P. L. Voss, M.-A. di Forte-Poisson, J.-C. De Jaeger, and A. Ougazzaden, Appl. Phys. Lett. **100**, 243503 (2012).

[30] V. Vezin, S. Yatagai, H. Shiraki, and S. Uda, Jpn. J. Appl. Phys. **36**, L1483 (1997).

[31] A. Y. Polyakov, M. Shin, M. Skowronski, D. W. Greve, R. G. Wilson, A. V. Govorkov, and R. M. Desrosiers, J. Electron. Mater. **26**, 237 (1997).

[32] C. H. Wei, Z. Y. Xie, J. H. Edgar, K. C. Zeng, J. Y. Lin, H. X. Jiang, C. Ignatiev, J. Chaudhuri, and D. N. Braski, MRS Proc. **537**, G3.79 (1998).

[33] G. Orsal, N. Maloufi, S. Gautier, M. Alnot, A. A. Sirenko, M. Bouchaour, and A. Ougazzaden, J. Cryst. Growth **310**, 5058 (2008).

[34] C. H. Wei and J. H. Edgar, J. Cryst. Growth **217**, 109 (2000).

[35] T. Akasaka and T. Makimoto, Appl. Phys. Lett. **88**, 1 (2006).

[36] N. Kobayashi, T. Makimoto, Y. Yamauchi, and Y. Horikoshi, J. Appl. Phys. **66**, 640

(1989).

[37] X. Li, S. Wang, H. Liu, F. A. Ponce, T. Detchprohm, and R. D. Dupuis, Phys. Status Solidi B **254**, 1600699 (2017).

[38] V. L. Solozhenko, D. Häusermann, M. Mezouar, and M. Kunz, Appl. Phys. Lett. **72**, 1691 (1998).

[39] N. P. Barradas, C. García Núñez, A. Redondo-Cubero, G. Shen, P. Kung, and J. L. Pau, Nucl. Instruments Methods Phys. Res. Sect. B Beam Interact. with Mater. Atoms **371**, 116 (2016).

[40] L. R. Doolittle, Nucl. Inst. Methods Phys. Res. B **9**, 344 (1985).

[41] S. Dai, J. Zhao, M. R. He, H. Wu, L. Xie, and J. Zhu, J. Phys. Chem. C **117**, 12895 (2013).

[42] Z. Chen, C. Cao, and H. Zhu, Chem. Vap. Depos. **13**, 527 (2007).

[43] A. Béré and A. Serra, Phys. Rev. B **68**, 1 (2003).

[44] V. Serin, C. Colliex, R. Brydson, S. Matar, and F. Boucher, Phys. Rev. B **58**, 5106 (1998).

[45] I. Ho and G. Stringfellow, Appl. Phys. Lett. **69**, 2701 (1996).

[46] A. M. Fischer, Y. O. Wei, F. A. Ponce, M. Moseley, B. Gunning, and W. A. Doolittle, Appl. Phys. Lett. **103**, 1 (2013).

[47] H. Fujii, C. Kisielowski, J. Krueger, M. S. H. Leung, R. Klockenbrink, M. Rubin, and E. R. Weber, MRS Proc. **449**, 227 (1996).

[48] B. Daudin, F. Widmann, G. Feuillet, Y. Samson, M. Arlery, and J. L. Rouviere, Phys. Rev. B **56**, 7069 (1997).

[49] C. Stampfl and C. G. Van de Walle, Phys. Rev. B **65**, 155212 (2002).

[50] G. Rocker, J. A. Schaefer, and W. Göpel, Phys. Rev. B **30**, 3704 (1984).

[51] U. Bangert, A. J. Harvey, R. Jones, C. J. Fall, A. T. Blumenau, R. Briddon, M. Schreck, and F. Hörmann, New J. Phys. **6**, 184 (2004).

[52] Z. W. Wang, Z. Y. Li, S. J. Park, A. Abdela, D. Tang, and R. E. Palmer, Phys. Rev. B **84**, 073408 (2011).

[53] W. Bi, H.-C. Kuo, P.-C. Ku, and B. Shen, *Handbook of GaN Semiconductor Materials and Devices* (Taylor & Francis Group, CRC press, Boca Raton, 2017), pp. 101, 107.

[54] G. Kresse and J. Hafner, Phys. Rev. B **47**, 558 (1993).

[55] G. Kresse and J. Furthmüller, Phys. Rev. B **54**, 11169 (1996).

[56] M. R. Krames, O. B. Shchekin, R. Mueller-Mach, G. O. Mueller, L. Zhou, G. Harbers, and M. G. Craford, J. Disp. Technol. **3**, 160 (2007).

[57] S. Nakamura, M. Senoh, S. Nagahama, N. Iwasa, T. Yamada, T. Matsushita, Y. Sugimoto, and H. Kiyoku, Appl. Phys. Lett. **69**, 4056 (1996).

[58] O. Jani, I. Ferguson, C. Honsberg, and S. Kurtz, Appl. Phys. Lett. **91**, 132117 (2007).

[59] C. J. Neufeld, N. G. Toledo, S. C. Cruz, M. Iza, S. P. DenBaars, and U. K. Mishra, Appl. Phys. Lett. **93**, 143502 (2008).

[60] C. H. Kunsman, J. Am. Chem. Soc. **50**, 2100 (1928).

[61] S. Nakamura, Jpn. J. Appl. Phys. **30**, 1705 (1991).

[62] K. G. Fertitta, A. L. Holmes, F. J. Ciuba, R. D. Dupuis, and F. A. Ponce, J. Electron. Mater. **24**, 257 (1995).

[63] F. A. Ponce, D. P. Bour, W. Götz, N. M. Johnson, H. I. Helava, I. Grzegory, J. Jun, and S. Porowski, Appl. Phys. Lett. **68**, 917 (1996).

[64] W. A. Harrison, *Electronic Structure and the Properties of Solids* (W. H. Freeman, San Francisco, 1980), p. 176.

[65] F. A. Ponce, S. Srinivasan, A. Bell, L. Geng, R. Liu, M. Stevens, J. Cai, H. Omiya, H. Marui, and S. Tanaka, Phys. Status Solidi B **240**, 273 (2003).

[66] A. Koukitu and Y. Kumagai, J. Phys. Condens. Matter **13**, 6907 (2001).

[67] S. Srinivasan, L. Geng, R. Liu, F. A. Ponce, Y. Narukawa, and S. Tanaka, Appl. Phys. Lett. **83**, 5187 (2003).

[68] R. Liu, J. Mei, S. Srinivasan, H. Omiya, F. A. Ponce, D. Cherns, Y. Narukawa, and T. Mukai, Jpn. J. Appl. Phys. **45**, L549 (2006).

[69] F. A. Ponce, D. Cherns, W. T. Young, and J. W. Steeds, Appl. Phys. Lett. **69**, 770 (1996).

[70] J. Mei, S. Srinivasan, R. Liu, F. A. Ponce, Y. Narukawa, and T. Mukai, Appl. Phys. Lett. **88**, 141912 (2006).

[71] F. Y. Meng, H. McFelea, R. Datta, U. Chowdhury, C. Werkhoven, C. Arena, and S. Mahajan, J. Appl. Phys. **110**, 073503 (2011).

[72] Y. A. Osipyan and I. S. Smirnova, J. Phys. Chem. Solids **32**, 1521 (1971).

[73] D. Gerthsen and C. B. Carter, Phys. Status Solidi A **136**, 29 (1993).

[74] Z. Wu, K. Nonaka, Y. Kawai, T. Asai, F. A. Ponce, C. Chen, M. Iwaya, S. Kamiyama, H. Amano, and I. Akasaki, Appl. Phys. Express **3**, 111003 (2010).

APPENDIX I

LIST OF PUBLICATIONS DURING PH.D. DISSERTATION RESEARCH

S. Wang, X. Hongen, H. Liu, A. M. Fischer, H. McFavilen, and F. A. Ponce, "Dislocation baskets in thick $In_xGa_{1-x}N$ epilayers," Submitted to J. Appl. Phys. on May 29, 2018.

K. Mehta, Y.S. Liu, J. Wang, H. Jeong, T. Detchprohm, Y.J. Park, S.R. Alugubelli, S. Wang, F.A. Ponce, S.C. Shen, and R.D. Dupuis, "Lateral Current Spreading in III-N Ultraviolet Vertical-Cavity Surface-Emitting Lasers Using Modulation-Doped Short Period Superlattices," IEEE J. Quantum Electron. **54**, 1 (2018).

K. Mehta, T. Detchprohm, Y.J. Park, Y.S. Liu, O. Moreno, S.R. Alugubelli, S. Wang, F.A. Ponce, S.C. Shen, R.D. Dupuis, and P.D. Yoder, "High Reflectivity Hybrid AlGaN/Silver Distributed Bragg Reflectors for Use in the UV-Visible Spectrum," IEEE J. Quantum Electron. **53**, 1 (2017).

S. Wang, X. Li, A. M. Fischer, T. Detchprohm, R. D. Dupuis, and F. A. Ponce, "Crystal structure and composition of BAlN thin films: Effect of boron concentration in the gas flow," J. Cryst. Growth, **475**, 334 (2017).

X. Li, S. Wang, H. Liu, F. A. Ponce, T. Detchprohm, and R. D. Dupuis, "100-nm thick single-phase wurtzite BAlN films with boron contents over 10%," Phys. Status Solidi B **254**, 1600699 (2017).

S. Zhao, J. Gao, S. Wang, H. Xie, F. A. Ponce, S. Goodnick, and S. Chowdhury, "Stability of alloyed and nonalloyed ohmic contacts to n-type GaN at high temperature in air," Jpn. J. Appl. Phys. **56**, 126502 (2017).

T. Detchprohm, Y.-S. Liu, K. Mehta, S. Wang, H. Xie, T.-T. Kao, S.-C. Shen, P. D. Yoder, F. A. Ponce, and R. D. Dupuis, "Sub 250 nm deep-UV AlGaN/AlN distributed Bragg reflectors," Appl. Phys. Lett. **110**, 011105 (2017).

A. M. Fischer, S. Wang, F. A. Ponce, B. P. Gunning, C. A. M. Fabien, and W. A. Doolittle, "Origin of high hole concentrations in Mg-doped GaN films," Phys. Status Solidi B **254**, 1600668 (2017).

S. Zhao, H. McFavilen, S. Wang, F. A. Ponce, C. Arena, S. Goodnick, and S. Chowdhury, "Temperature Dependence and High-Temperature Stability of the Annealed Ni/Au Ohmic Contact to *p*-Type GaN in Air," J. Elec. Mater. **45**, 2087 (2016).

Y.-S. Liu, S. Wang, H. Xie, T.-T. Kao, K. Mehta, X. J. Jia, S.-C. Shen, P. D. Yoder, F. A. Ponce, T. Detchprohm, and R. D. Dupuis, "Strain management of AlGaN-based distributed Bragg reflectors with GaN interlayer grown by metalorganic chemical vapor deposition," Appl. Phys. Lett. **109**, 081103 (2016).

Y.-S. Liu, A. F. M. Haq, K. Mehta, T.-T. Kao, S. Wang, H. Xie, S.-C. Shen, P. D. Yoder, F. A. Ponce, T. Detchprohm, and R. D. Dupuis, "Optically pumped vertical-cavity surface-emitting laser at 374.9nm with an electrically conducting n-type distributed Bragg reflector," Appl. Phys. Exp. **9**, 111002 (2016).

X. Li, S. Wang, H. Xie, Y. O. Wei, T.-T. Kao, Md. D. Satter, S.-C. Shen, P. D. Yoder, T. Detchprohm, R. D. Dupuis, A. M. Fischer, and F. A. Ponce, "Growth of high-quality AlN layers on sapphire substrates at relatively low temperatures by metalorganic chemical vapor deposition," Phys. Status Solidi B **252**, 1089 (2015).

X. Li, Y. O. Wei, S. Wang, H. Xie, T.-T. Kao, Md. D. Satter, S.-C. Shen, P. D. Yoder, T. Detchprohm, R. D. Dupuis, A. M. Fischer, and F. A. Ponce, "Temperature dependence of the crystalline quality of AlN layer grown on sapphire substrates by metal organic chemical vapor deposition," J. Cryst. Growth, **414**, 76 (2015).

B. P. Gunning, C. A. M. Fabien, J. J. Merola, E. A. Clinton, W. A. Doolittle, S. Wang, A. M. Fischer, and F. A. Ponce, "Comprehensive study of the electronic and optical behavior of highly degenerate p-type Mg-doped GaN and AlGaN," J. Appl. Phys. **117**, 045710 (2015).

X. Li, T.-T. Kao, Md. M. Satter, Y. O. Wei, S. Wang, H. Xie, S.-C. Shen, P. D. Yoder, A. M. Fischer, F. A. Ponce, T. Detchprohm, and R. D. Dupuis, "Demonstration of transverse-magnetic deep-ultraviolet stimulated emission from AlGaN multiple-quantum-well lasers grown on a sapphire substrate," Appl. Phys. Lett. **106,** 041115 (2015).

X. Li, T. Detchprohm, T.-T. Kao, Md. M. Satter, S.-C. Shen, P. D. Yoder, R. D. Dupuis, S. Wang, Y. O. Wei, H. Xie, A. M. Fischer, F. A. Ponce, T. Wernicke, C. Reich, M. Martens, and M. Kneissl, "Low-threshold stimulated emission at 249nm and 256nm from AlGaN-based multiple-quantum-well lasers grown on sapphire substrates," Appl. Phys. Lett. **105**, 141106 (2014).